Supplementary Information for:

Cerium(IV) Complexes with Guanidinate Ligands: Intense Colors and Anomalous Electronic Structures

Yusen Qiao,[1,2] Haolin Yin,[1] Liane M. Moreau,[2] Rulin Feng,[3] Robert F. Higgins,[1] Brian C. Manor,[1] Patrick J. Carroll,[1] Corwin H. Booth,[2] Jochen Autschbach,[3] and Eric J. Schelter[1,*]

[1]*P. Roy and Diana T. Vagelos Laboratories, Department of Chemistry, University of Pennsylvania, 231 South 34 Street, Philadelphia, Pennsylvania 19104, United States*
[2]*Chemical Sciences Division, Lawrence Berkeley National Laboratory, Berkeley, California 94720, United States*
[3]*Department of Chemistry, University at Buffalo, State University of New York, Buffalo, New York 14260, United States*

E-mail: schelter@sas.upenn.edu

1. Materials and Methods

Safety Considerations. *No unexpected hazards were noted through the syntheses and characterizations performed in the current work.*

General Methods. All reactions and manipulations were performed under an inert atmosphere (N_2) using standard Schlenk techniques or in a Vacuum Atmospheres, Inc. Nexus II drybox equipped with a molecular sieves 13X/Q5 Cu–0226S catalyst purifier system. Glassware was oven-dried for 3 hours at 150 °C prior to use. ^{1}H NMR, ^{13}C NMR, and ^{19}F NMR spectra were obtained on a Bruker DMX–300 Fourier transform NMR spectrometer at 300 MHz, 91 MHz, and 282 MHz. Chemical shifts were recorded in units of parts per million referenced to residual solvent peaks (^{1}H), characteristic solvent peaks (^{13}C{^{1}H}), or an internal solution standard of fluorobenzene at –113.15 ppm (^{19}F). The electronic absorption spectra were obtained using a Perkin Elmer 950 UV-vis/NIR spectrophotometer. All samples were prepared in 1 mm pathlength quartz cuvettes with screw cap under an N_2 atmosphere. Fitting of the UV-vis spectra was performed using fityk.[1] Elemental analyses were performed at Midwest Microlab, Inc.

Materials. Toluene, THF, CH_2Cl_2, hexanes, and *n*-pentane were purchased from Fisher Scientific. The solvents were sparged for 20 min with dry N_2 and dried using a commercial two column solvent purification system comprising columns packed with Q5 reactant and neutral alumina respectively (for hexanes and *n*-pentane), or two columns of neutral alumina (for toluene, THF and CH_2Cl_2). Deuterated solvents were purchased from Cambridge Isotope Laboratories, Inc. and stored over molecular sieves overnight prior to use. Ph_3CCl was purchased from Acros Organics and used as received. $Ce[N(SiMe_3)_2]_3Cl$ (**1-Cl**),[2,3] $[(Me_3Si)_2NC(N^iPr)_2]CeCl[N(SiMe_3)_2]_2$ (**2-Cl**),[4] $[(Me_3Si)_2NC(N^iPr)_2]_3Ce$ (**4**),[5] $\{[(Me_3Si)_2NC(N^iPr)_2]_3Ce[BAr^F_4]$ (**[4$^+$][BAr$^F_4$]**, Ar^F = 3,5-bis(trifluoromethyl)phenyl),[5] $[Cp_2Fe][BAr^F_4]$,[6] and $[^nPr_4N][BAr^F_4]$[7] were prepared according to reported procedures. Crystal structures have been uploaded to the CCDC with these identifiers: CCDC 1965035−1965036.

2. Synthetic Details and Characterizations

Synthesis of **[3$^+$][BAr$^F_4$]**. To a vial containing [(Me$_3$Si)$_2$NC(N^{i}Pr)$_2$]$_2$Ce^{III}[N(SiMe$_3$)$_2$] (0.087 g, 0.100 mmol, 1.00 equiv) dissolved in 2 mL CH_2Cl_2, [Cp$_2$Fe][BAr$^F_4$] (0.105 g, 0.100 mmol, 1.00 equiv) was added, leading to an immediate color change to dark green. After stirring for 12 h, the mixture was filtered through a pipette filter packed with Celite. The filtrate was layered with 3 mL *n*-pentane and stored at –25 °C overnight leading to precipitation of green solids. The mixture was filtered through a pipette filter packed with Celite to remove the by-products. The volatiles of filtrate were removed under reduced pressure. The resulting dark green solids were collected by filtration over a medium porosity fritted filter and washed with 3 × 5 mL *n*-pentane. The solids were dried under reduced pressure for 1 h. Yield: 0.088 g, 0.051 mmol, 51%. ^{1}H NMR (CD_2Cl_2, 500 MHz, 300 K): δ 7.71 (s, 8H, –Ar), 7.54 (s, 4H, –Ar), 4.88 (m, 4H, –CH^{iPr}), 1.43 (m, 24H, –CH$_3^{iPr}$), 0.54 (s, 18 H, –SiMe$_3$), 0.28 (s, 36 H, –SiMe$_3$). ^{13}C{^{1}H} NMR (CD_2Cl_2, 126 MHz, 300 K): δ = 168.39, 162.34 (q, $^1J_{B\text{-}C}$, 31.7 Hz), 135.4 (s), 129.6 (q, $^2J_{C\text{-}F}$, 19.8 Hz), 125.2 (q, $^1J_{C\text{-}F}$, 172 Hz), 118.0 (s), 51.83 (s), 30.07 (s), 4.79 (s), 3.23 (s). ^{19}F NMR (CD_2Cl_2, 300 MHz, 300 K): δ −62.14 (s, 24F, –CF$_3$). Elemental analysis found (calculated) for $C_{64}H_{94}BCeF_{24}N_7Si_6$: C, 44.33 (44.26), H, 5.47 (5.46), N, 5.47 (5.65). Single crystals suitable for X-ray analysis were obtained by a CH_2Cl_2/toluene layering of the product.

Synthesis of **2-Cl$^-$**. To a vial containing [(Me$_3$Si)$_2$NC(N^{i}Pr)$_2$]Ce^{III}[N(SiMe$_3$)$_2$]$_2$ (0.075 g, 0.100 mmol, 1.00 equiv) dissolved in 1 mL CH_2Cl_2, a 1 mL CH_2Cl_2 solution containing NEt$_4$Cl (0.017 g, 0.100 mmol, 1.00 equiv) was added leading to an immediate color change from bright yellow to colorless. After stirring for 3 h, the clear solution was filtered through Celite packed in a pipette filter and layered with 8 mL pentane. Storage of the layered solution at -25 °C overnight led to the formation of colorless crystalline solids. The products were collected on a medium size fritted filter and dried under reduced vacuum for 1 h. Yield: 0.068 g, 0.075 mmol, 75%. ^{1}H NMR (C_6D_6, 300 MHz, 300 K): δ 14.78 (br, 2H, –CHMe$_2^{iPr}$), 6.53 (br, 12H, –CH$_3^{iPr}$), 1.44 (m, 8H, –CH$_2^{Et}$), 1.22 (s, 18H, –SiMe$_3$), 0.01 (t, 12H, –CH$_3^{Et}$, J = 4.5 Hz), –4.43 (s, 36H, –SiMe$_3$). Elemental analysis found

(calculated) for $C_{33}H_{88}CeClN_6Si_6$: C, 43.15(43.40), H, 9.67(9.71), N, 9.16(9.20). Single crystals suitable for X-ray analysis were obtained through the same method.

3. NMR Spectra

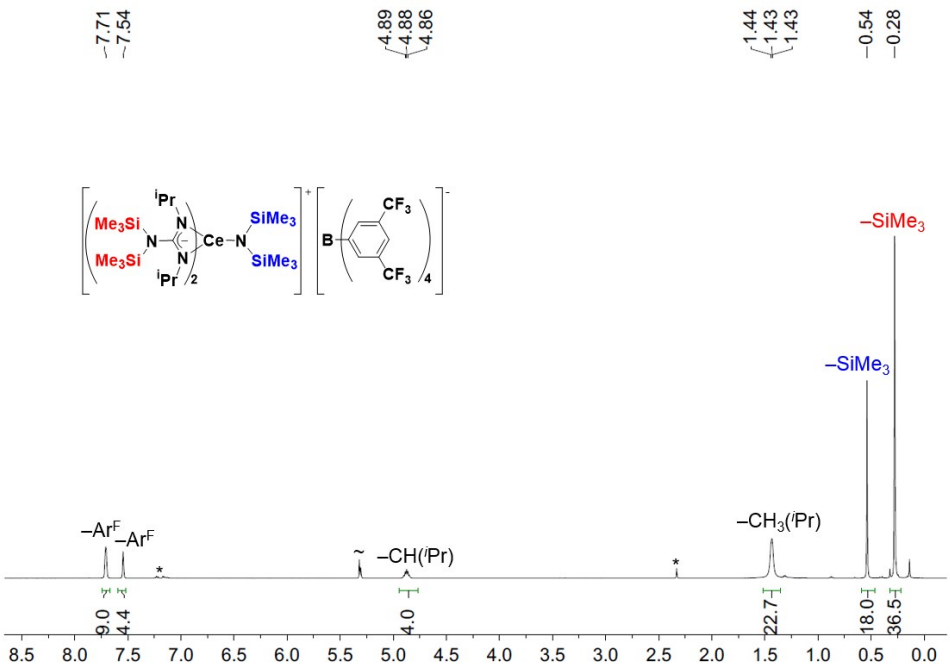

Figure S1. ^{1}H NMR spectrum of **{[(Me$_3$Si)$_2$NC(N^{i}Pr)$_2$]$_2$Ce^{IV}[N(SiMe$_3$)$_2$]}[BAr$^F_4$] ([3$^+$][BAr$^F_4$])** in CD_2Cl_2. Residue toluene is noted as *. Proteo- residue peaks of $CDHCl_2$ is noted as ~.

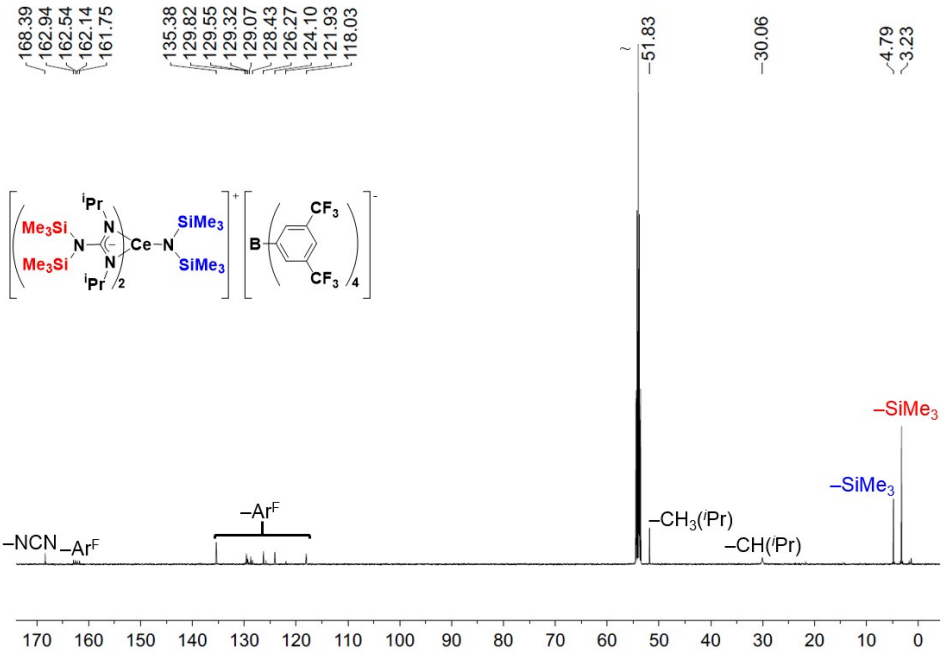

Figure S2. ^{13}C NMR spectrum of **{[(Me$_3$Si)$_2$NC(N^{i}Pr)$_2$]$_2$Ce^{IV}[N(SiMe$_3$)$_2$]}[BAr$^F_4$] ([3$^+$][BAr$^F_4$])** in CD_2Cl_2. Proteo- residue peaks of $CDHCl_2$ is noted as ~.

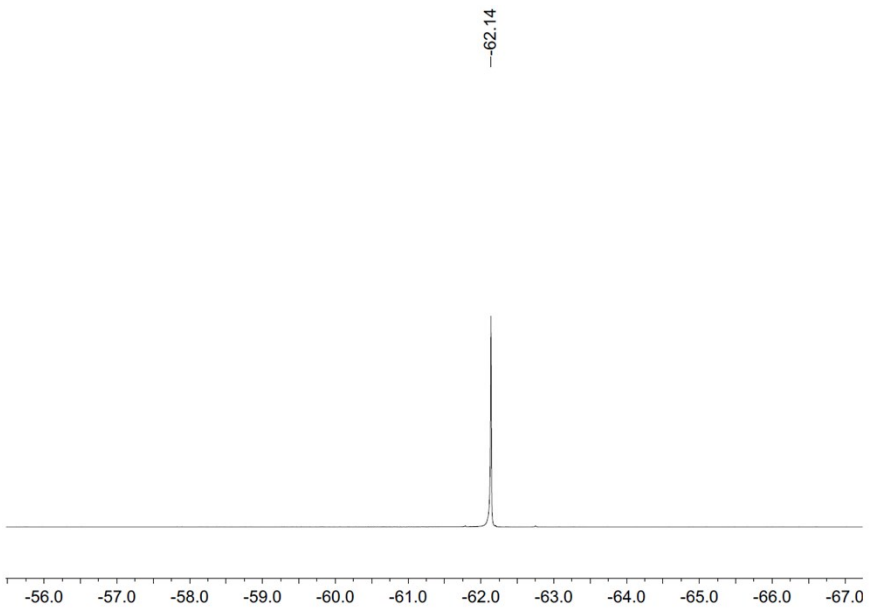

Figure S3. ^{19}F NMR spectrum of **{[(Me$_3$Si)$_2$NC(N^{i}Pr)$_2$]$_2$Ce^{IV}[N(SiMe$_3$)$_2$]}[BAr$^F{}_4$] ([3$^+$][BAr$^F{}_4$])** in CD_2Cl_2.

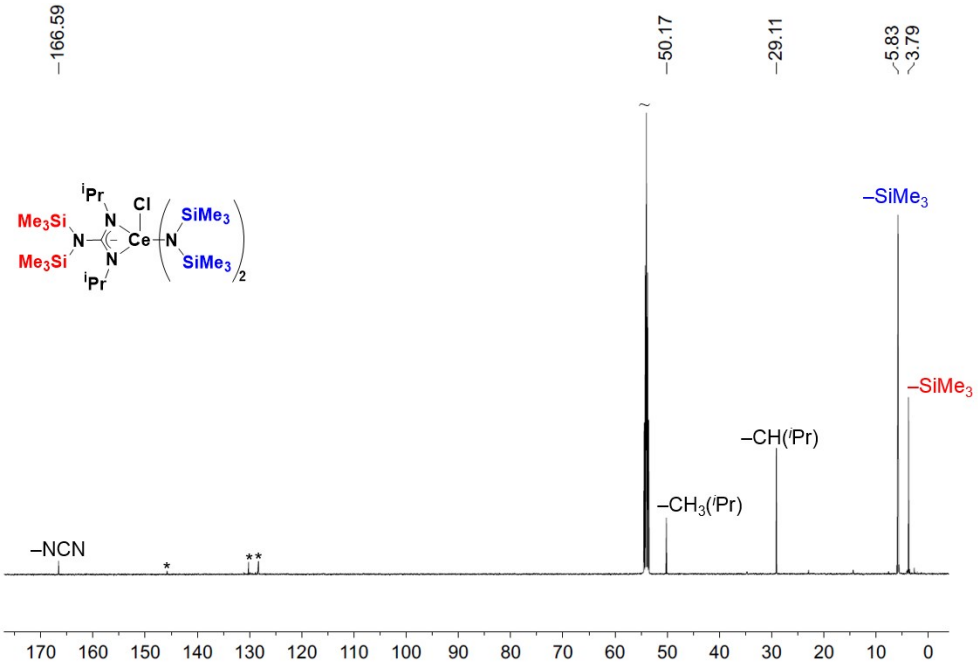

Figure S4. ^{13}C NMR spectrum of **[(Me$_3$Si)$_2$NC(N^{i}Pr)$_2$]$_2$Ce^{IV}Cl[N(SiMe$_3$)$_2$]$_2$ (2-Cl)** in CD_2Cl_2. Proteo- residue peaks of $CDHCl_2$ is noted as ~ and a small amount of Gomberg's dimer impurity is noted as *.

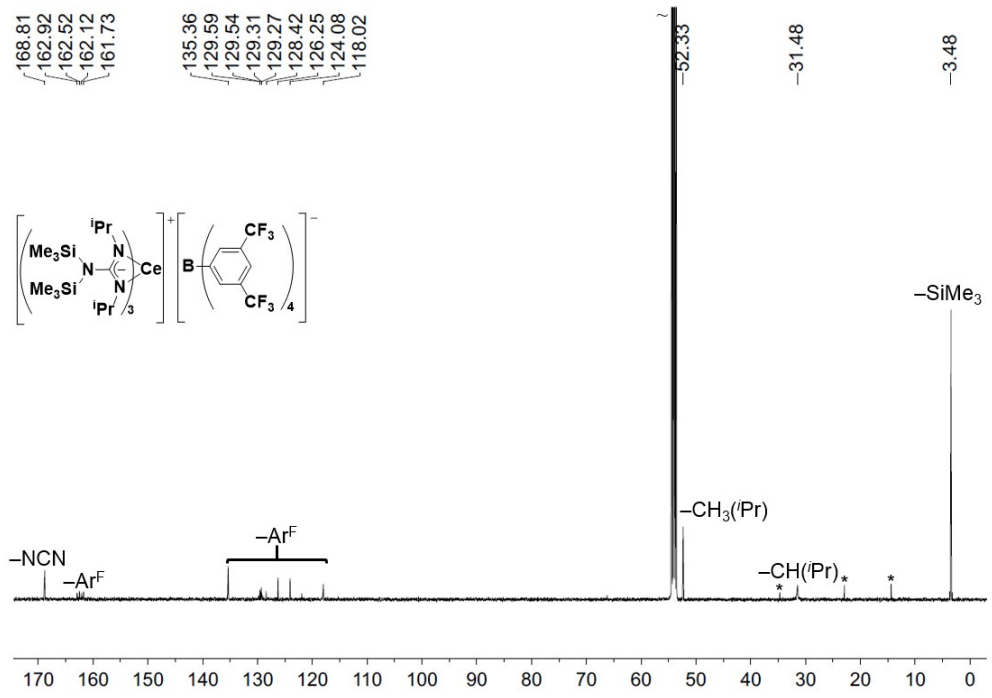

Figure S5. ^{13}C NMR spectrum of **{[(Me$_3$Si)$_2$NC(N^{i}Pr)$_2$]$_3$Ce^{IV}} [BAr$^F_4$] ([4$^+$][BAr$^F_4$])** in CD_2Cl_2. Proteo- residue peaks of $CDHCl_2$ is noted as ~ and residue *n*-pentane is noted as *.

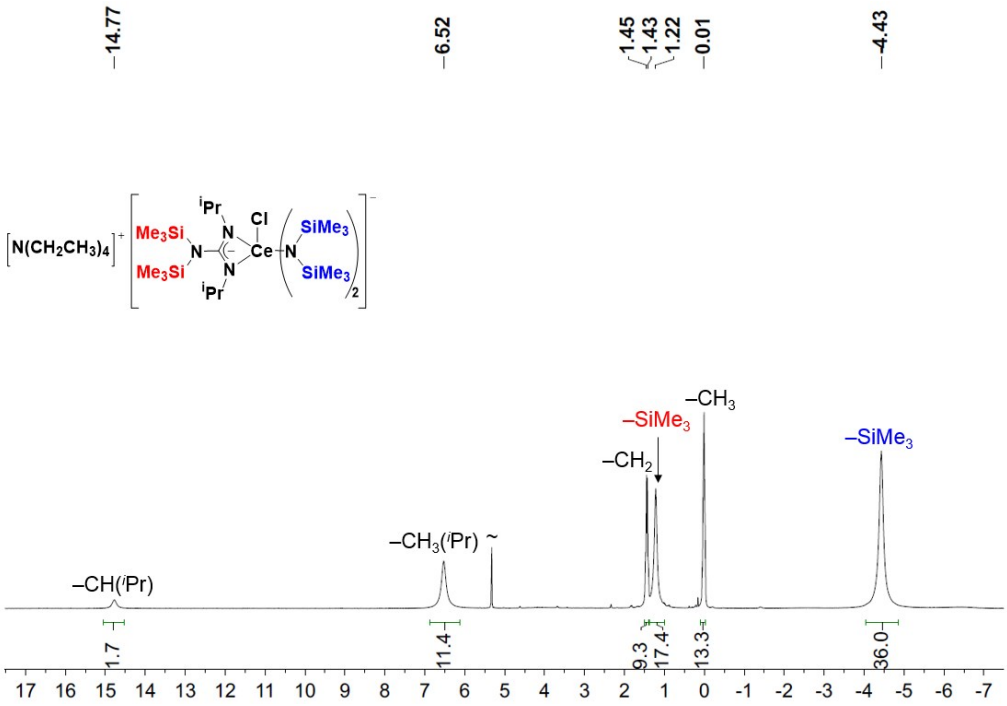

Figure S6. ^1H NMR spectrum of **[NEt$_4$]{[(Me$_3$Si)$_2$NC(N^{i}Pr)$_2$]$_2$Ce^{III}Cl[N(SiMe$_3$)$_2$]$_2$} (2-Cl$^-$)** in CD_2Cl_2. Proteo- residue peaks of $CDHCl_2$ is noted as ~.

4. X-Ray Crystal Structures

X-ray intensity data were collected on a Bruker APEXII CCD area detector employing graphite-monochromated Mo-Kα radiation (λ=0.71073 Å) at a temperature of 100(1) K or 143(1) K. Preliminary indexing was performed from a series of thirty-six 0.5° rotation frames with exposures of 10 seconds. Following full data collection, rotation frames were integrated using SAINT,[8] producing a listing of unaveraged F^2 and $\sigma(F^2)$ values which were then passed to the SHELXTL[9] program package for further processing and structure solution. The intensity data were corrected for Lorentz and polarization effects and for absorption using SADABS[10] or TWINABS[11]. The structure was solved by direct methods (SHELXS-97[12]). Refinement was by full-matrix least squares based on F^2 using SHELXL-97.[12] All reflections were used during refinement. Non-hydrogen atoms were refined anisotropically and hydrogen atoms were refined using a riding model.

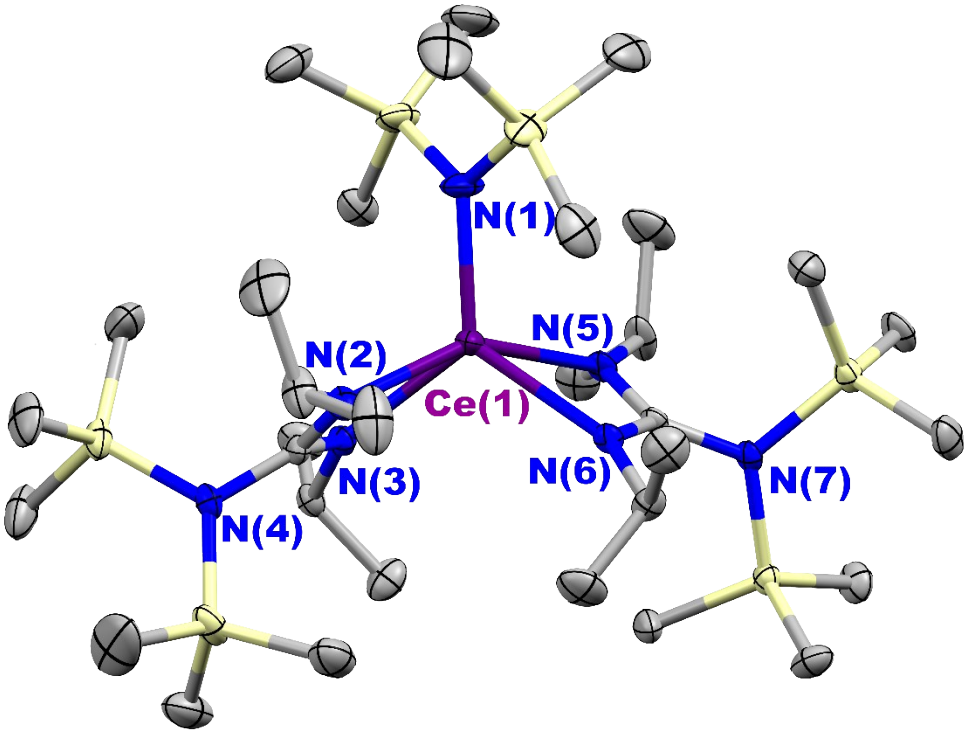

Figure S7. Thermal ellipsoid plot of **{[(Me$_3$Si)$_2$NC(N^{i}Pr)$_2$]$_2$Ce^{IV}[N(SiMe$_3$)$_2$]}[BAr$^F{}_4$] ([3$^+$][BAr$^F{}_4$])** at the 30% probability level. The [BAr$^F{}_4$]$^-$ anion was omitted for clarity.

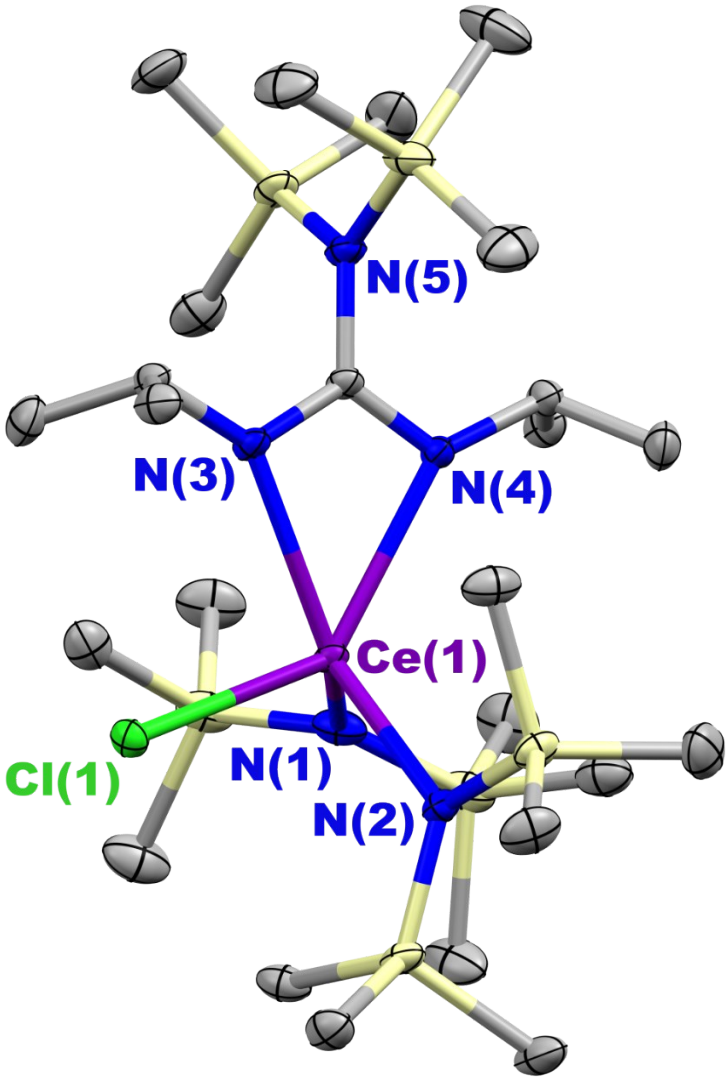

Figure S8. Thermal ellipsoid plot of **$[NEt_4]\{[(Me_3Si)_2NC(N^iPr)_2]_2Ce^{III}Cl[N(SiMe_3)_2]_2\}$ (2-Cl^-)** at the 30% probability level. Cation was omitted for clarity.

5. Electronic Absorption Spectra

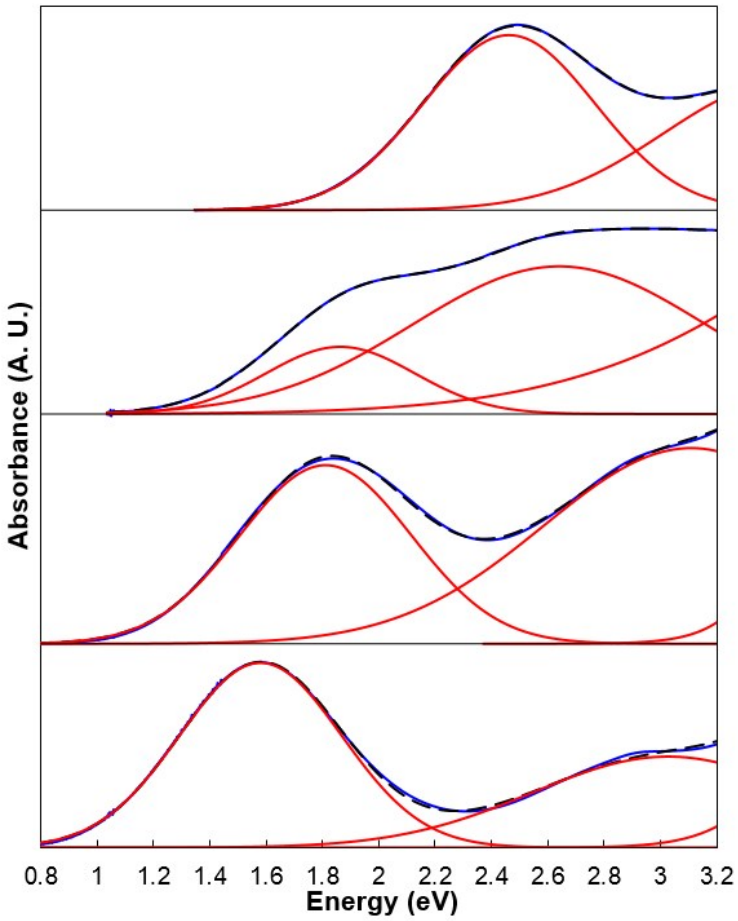

Figure S9. Fitting of absorption spectra of **1-Cl**, **2-Cl**, **[3^{+}][BAr$^{F}_{4}$]**, **[4^{+}][BAr$^{F}_{4}$]** plotted in eV. Two or three Gaussian bands (red solid lines) were applied for each fitting. Sum of the fit (blue solid lines) is in good agreement with experimental spectra (black dashed lines).

6. X-Ray Absorption Spectroscopy

XANES data at the Ce L_3-edge absorption edge were collected at Beamline 11-2 of the Stanford Synchrotron Radiation Lightsource using a Si 220 (φ = 0) monochromator detuned to 50 %. The vertical slit height was chosen so that the resolution of the data is core-hole lifetime limited. Data were collected in transmission and energy was calibrated by setting the first inflection point of the absorption of a CeO_2 standard to 5723 eV. Data were processed by subtracting a linear pre-edge background and normalizing to unity.

To prepare for data collection, powder samples were diluted with dry boron nitride and packed into the slots of an aluminum holder with aluminized mylar windows sealed with indium within an argon dry box to achieve absorption step heights (normalization factors in Figure 7) less than 0.33 to avoid thickness effect issues with the lineshape. Since the samples are air sensitive, they were kept under argon until measurement, and the sealed holder was exposed to air for less than one minute during transfer to vacuum. Samples were measured both at 50 K and 300 K using a liquid He-cooled cryostat to test the effect of temperature on the resulting spectra. An easily-oxidizable sample, $(C_5Me_4H)_3Ce$, was measured along with the samples to ensure that no O_2 had leaked into the sample holder during measurement.

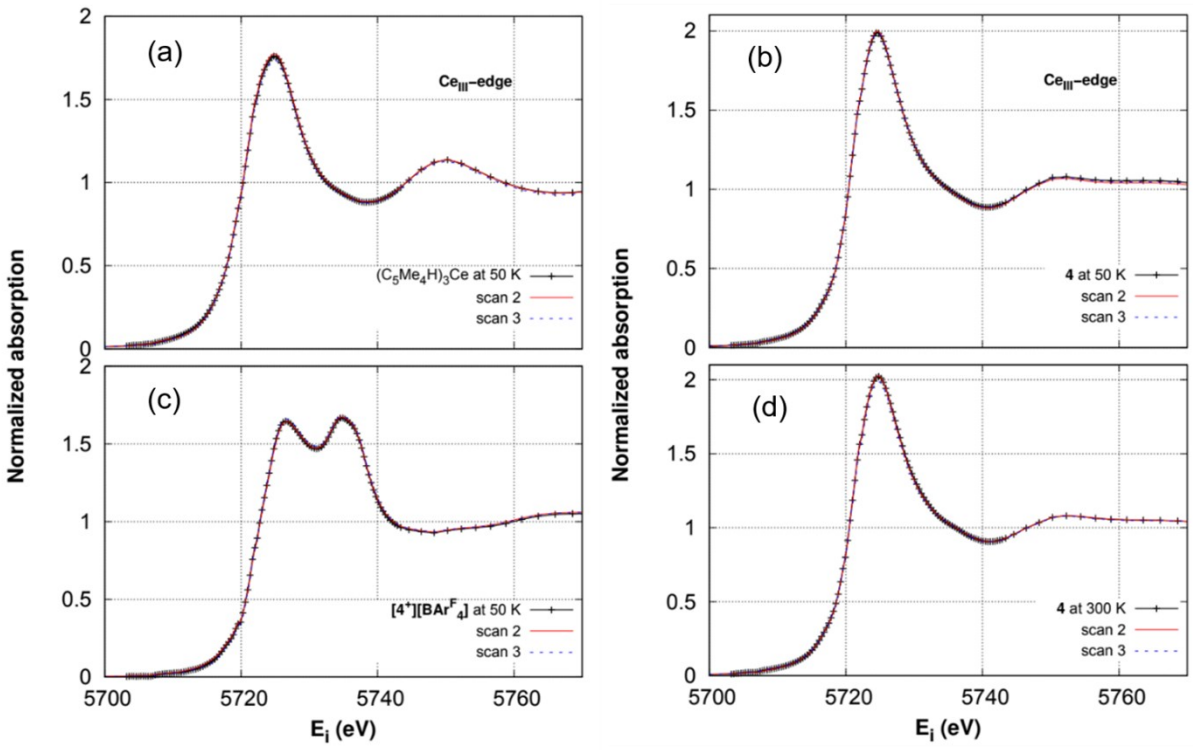

Figure S10. Confirmation of repeatability between XANES scans. The repeatability that we observe between XANES scans confirms that the oxidation state of the sample is not changing when exposed to the x-ray beam during the time frame required for measurement.

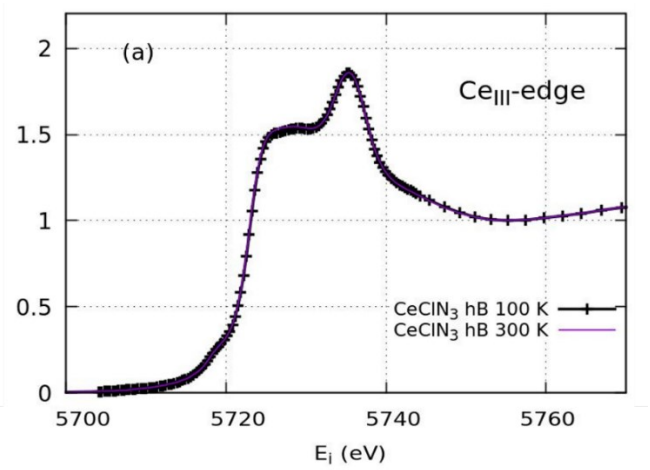

Figure S11. Plots of **1-Cl** confirm the Ce(IV) oxidation state. There is no temperature dependence to the oxidation states of the compound.

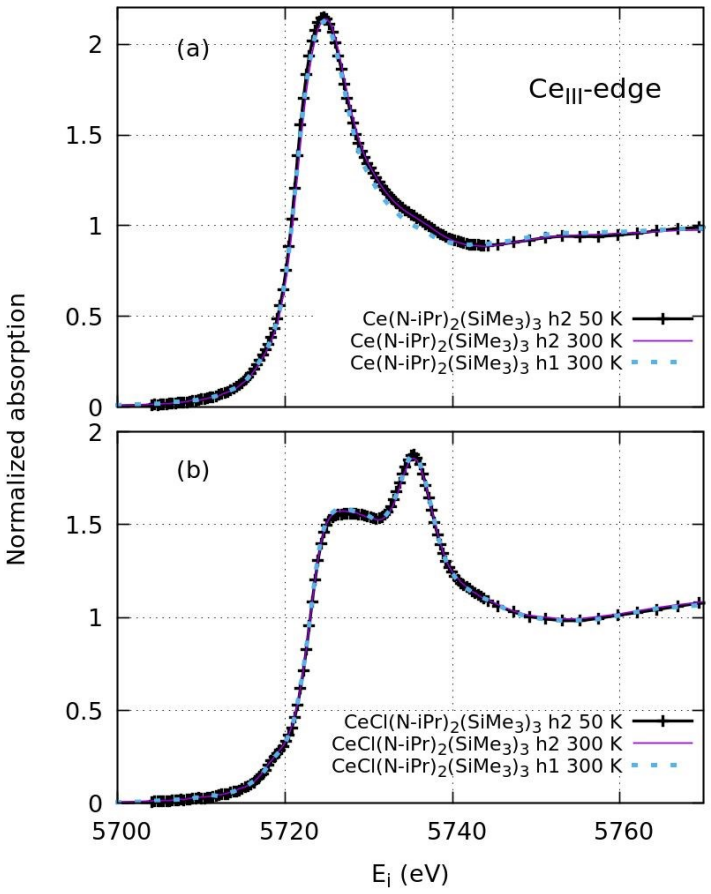

Figure S12. Plots of both **2** (a) and **2-Cl** (b) confirm the Ce(III) oxidation state in **2** and Ce(IV) oxidation state in **2-Cl**. There is no temperature dependence to the oxidation states of these compounds.

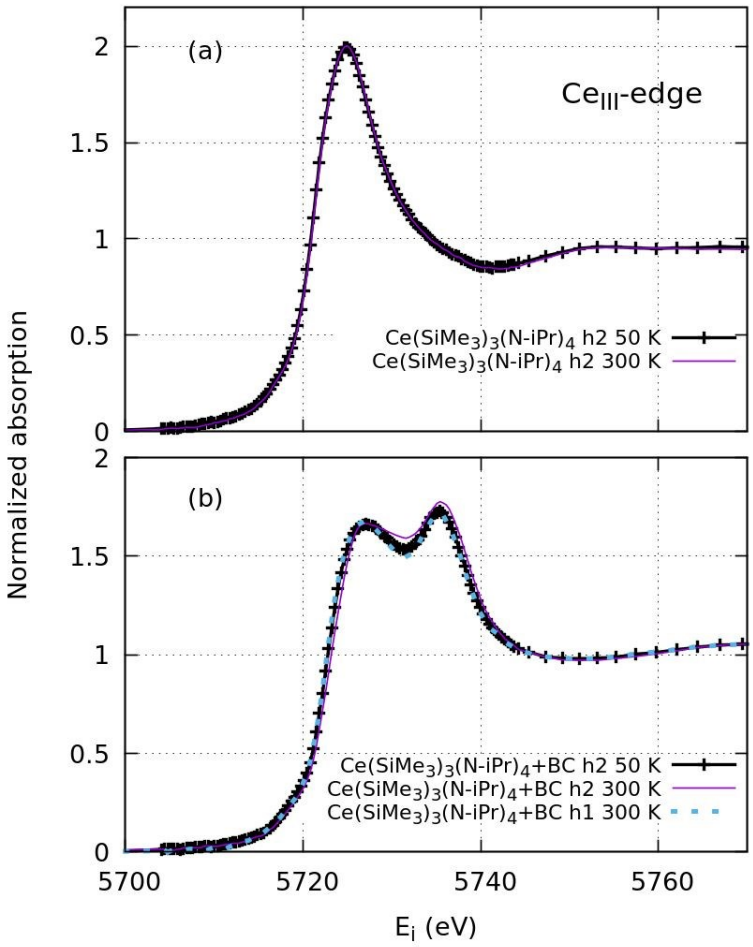

Figure S13. Plots of both **3** (a) and **[3$^+$][BAr$^F_4$]** (b) confirm the Ce(III) oxidation state in **3** and Ce(IV) oxidation state in **[3$^+$][BAr$^F_4$]**. There is no temperature dependence to the oxidation states of these compounds.

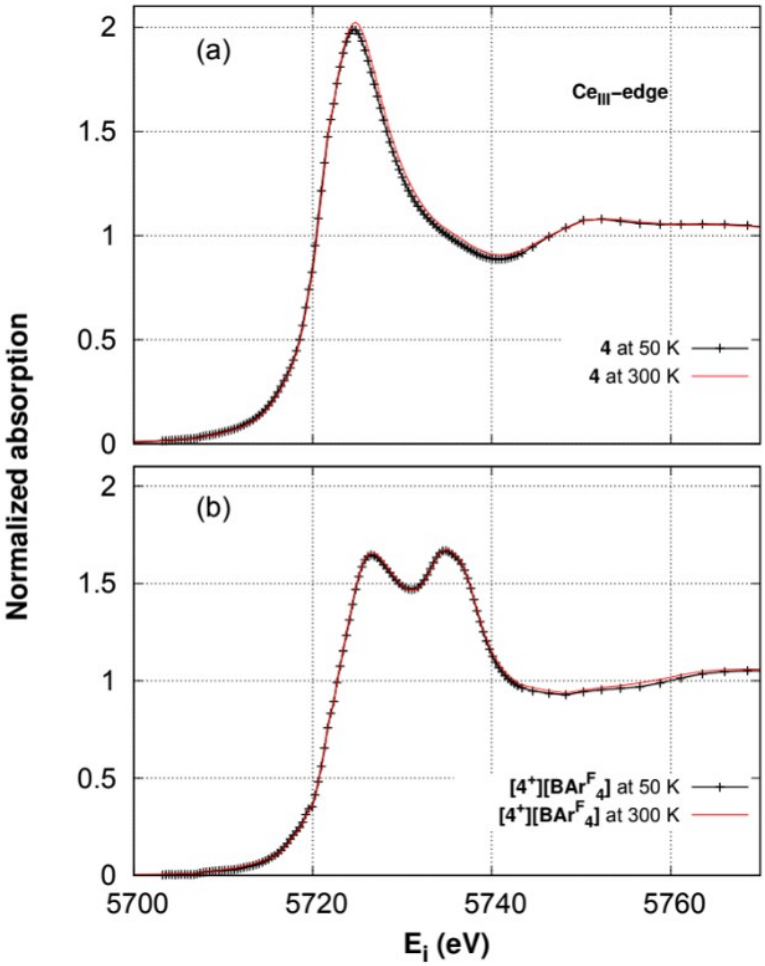

Figure S14. Plots of both **4** (a) and **[4$^+$][BAr$^F_4$]** (b) confirm that there is no temperature dependence to the oxidation states of these compounds. This is in agreement with the temperature-independent magnetism observed for **[4$^+$][BAr$^F_4$]**.

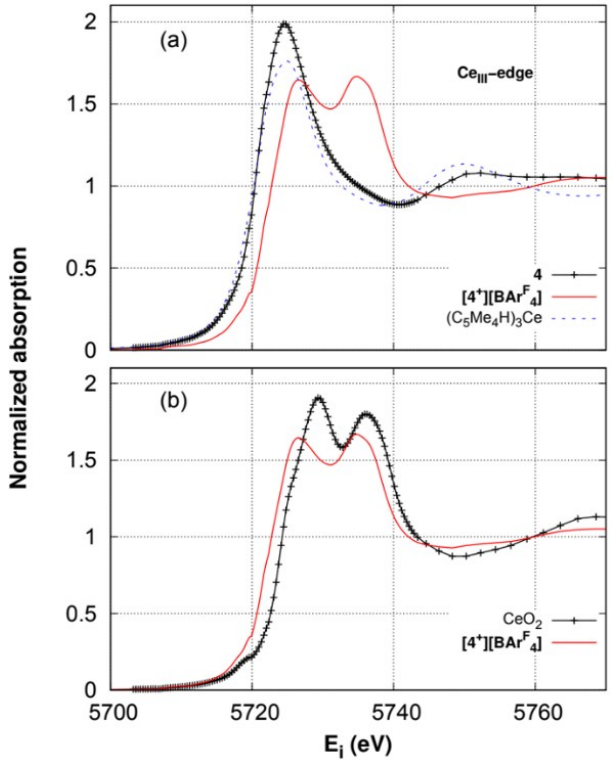

Figure S15. Normalized X-ray absorption spectra at the Ce L_{III} absorption edge. a) Plotting **[4$^+$][BAr$^F_4$]** (red) with the Ce^{III} complexes **4** (black) and $(C_5Me_4H)_3Ce$ (dashed) for comparison. b) Plotting **[4$^+$][BAr$^F_4$]** (red) with CeO_2 (black) confirms the formal Ce^{IV} oxidation state of **[4$^+$][BAr$^F_4$]**.

XANES data were fit according to previously described methodology[13-15] in order to determine n_f. The fits consisted of a sum of a step-like function to model the absorption edge and Gaussians associated with f1 and f0 peaks as well as a shoulder into the EXAFS region. The step-like function is a single continuum function with a weighted average of the peak energies of the f1 and f0 peaks, in order to reduce the number of parameters in the fit and to control correlations between the fit parameters. We define the step according to the expression:

$$\int_{-\infty}^{E} I_{edge} e^{\frac{-(E-E_0)^2}{2\sigma^2}} dE$$

and the Gaussians according to the expression:

$$I_i e^{\frac{-(E-e_i)^2}{2\sigma_i^2}}$$

where E is the incident energy, e_i is the peak energy, σ_i is the half-width of the Gaussian and I_i is the intensity of peak i. E_0 is constrained as the average of the peak energies of f1 and f0 weighted by the area under each associated Gaussian. The Gaussian widths of the f1 and f0 peaks were held equivalent.

Error bars for individual parameters were calculated using the covariance matrix assuming normal distributions for variances in the data. The error bars associated with n_f are fitted to be ±0.01, but our experience dictates an estimate of ±0.03. Parameters reported without error bars were held fixed during the fit. Results from the fit are shown in Figures S64 and S65 with parameters shown in Tables S15-S18.

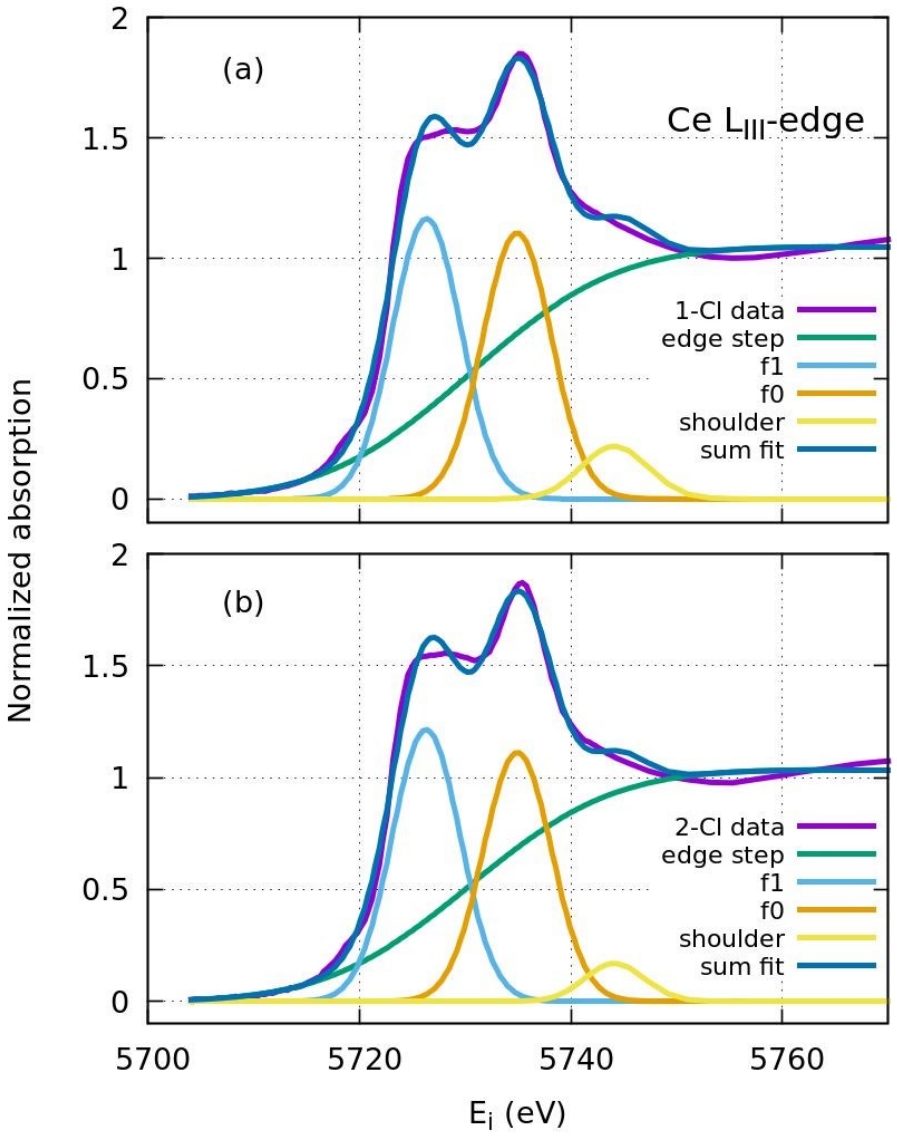

Figure S16. XANES data, fit and fit components for **1-Cl** (a) and **2-Cl** (b).

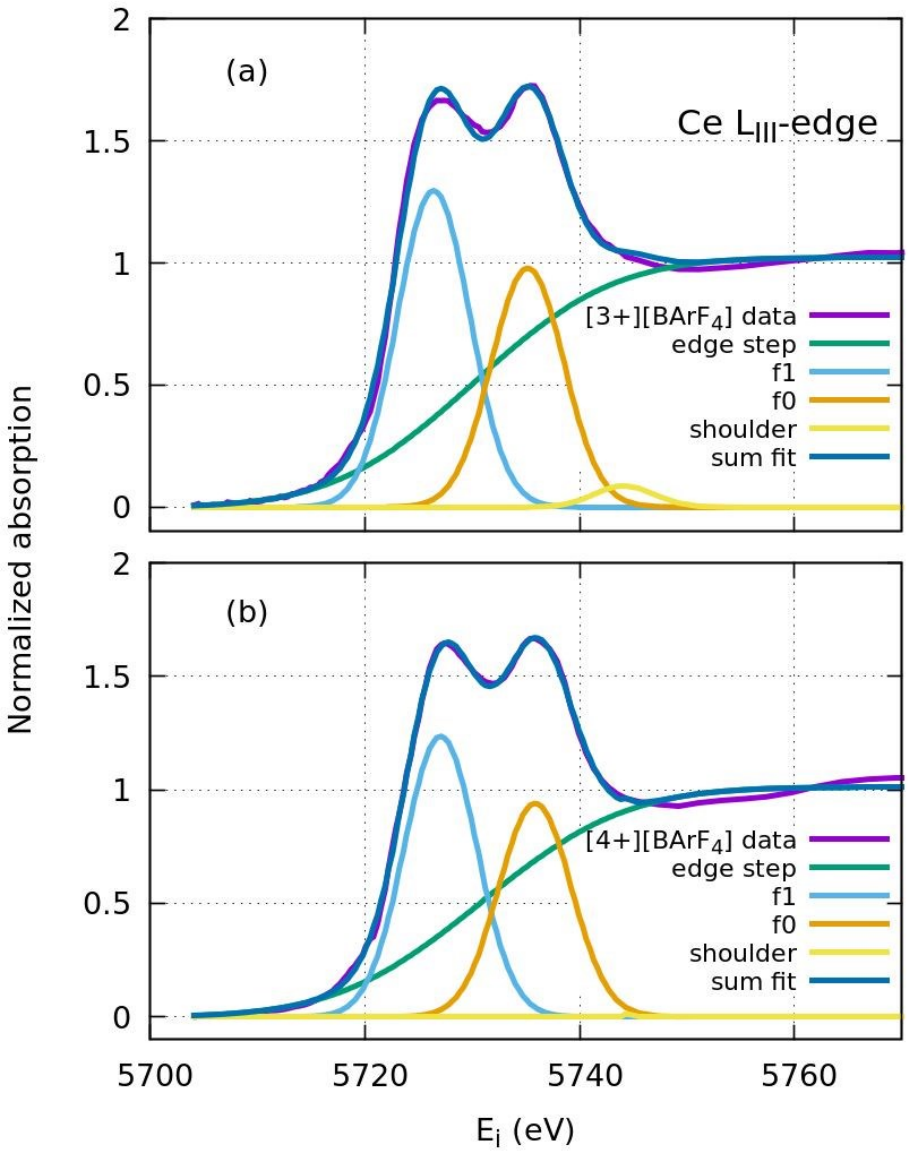

Figure S17. XANES data, fit and fit components for **[3$^+$][BAr$^F_4$]** (a) and **[4$^+$][BAr$^F_4$]** (b).

Table S1. Fit parameter results for the edge step continuum function.

Sample	**I_{edge}**	**E_0(eV)**	**σ_1(eV)**
1-Cl	0.038(2)	5730.53	10.9(5)
2-Cl	0.039(2)	5730.44	10.7(5)
[3^+][BAr^F_4]	0.040(1)	5730.17	10.3(4)
[4^+][BAr^F_4]	0.038(1)	5730.86	10.6(2)

Table S2. Fit parameter results for Gaussians fit to the f1, f0 and EXAFS shoulder (χ).

Sample	**a_{f1}**	**e_{f1} (eV)**	**σ_{f1}(eV)**	**a_{f0}**	**e_{f0} (eV)**	**σ_{f0}(eV)**	**a_χ**	**e_χ (eV)**	**σ_χ(eV)**
1-Cl	1.16(2)	5726.36(8)	3.24(8)	1.11(2)	5734.9(1)	3.24(8)	0.22(3)	5744.12	3.2(6)
2-Cl	1.21(2)	5726.31(7)	3.22(8)	1.11(2)	5734.9(1)	3.22(8)	0.17(3)	5744.12	2.8(6)
[3^+][BAr^F_4]	1.30(1)	5726.40(5)	3.36(5)	0.98(2)	5735.16(9)	3.36(5)	0.09(2)	5744.12	2.7(8)
[4+][BAr^F_4]	1.236(7)	5727.05(3)	3.37(3)	0.941(9)	5735.85(5)	3.37(3)	0.14	5744.12	0.08(2)

Table S3. n_f values calculated from XANES fitting. Areas under the f1 and f0 peaks as determined from XANES fitting using Gaussians are shown. These areas were in turn used to calculate nf, which represents the overall f occupancy of the respective complexes. Note that while the area errors are obtained from the fit, we apply a ±0.03 error to the n_f measurements, which is larger than the fitted ±0.01 value, as a better representation based on experience.

Sample	f1 area	f0 area	n_f
1-Cl	9.5 ± 0.3	9.0 ± 0.2	0.51 ± 0.01
2-Cl	9.8 ± 0.3	9.0 ± 0.2	0.52 ± 0.01
[3$^+$][BAr$^F_4$]	10.9 ± 0.2	8.3 ± 0.1	0.57 ± 0.01
[4$^+$][BAr$^F_4$]	10.5 ± 0.1	8.0 ± 0.1	0.57 ± 0.01

Table S4. R(%) values (goodness of fit) for the XANES fits

Sample	R(%) from Fit
1-Cl	2.9
2-Cl	3.1
[3$^+$][BAr$^F_4$]	1.9
[4$^+$][BAr$^F_4$]	1.4

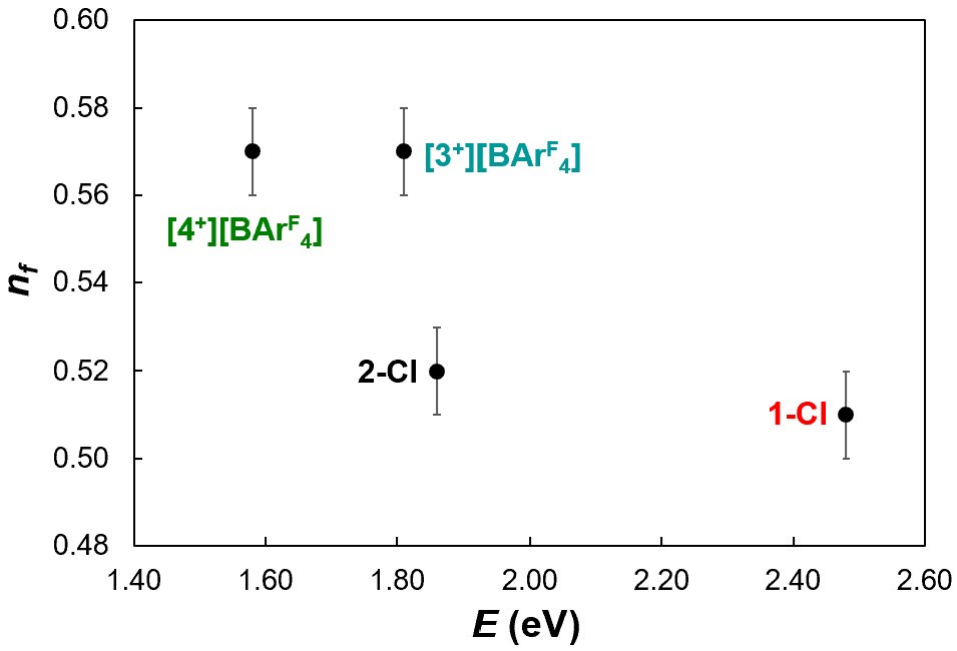

Figure S18. A plot of the energy of low-lying LMCT bands and the n_f value. Error bars were given for n_f values.

7. Electrochemistry

Cyclic voltammetry experiments were performed using a CH Instruments 620D Electrochemical Analyzer/Workstation and the data were processed using CHI software v 9.24. All experiments were performed in an N_2 atmosphere dry box using electrochemical cells that consisted of a 4 mL vial, a glassy carbon (2 mm diameter) working electrode, a platinum wire counter electrode, and a silver wire plated with AgCl as a quasi-reference electrode. The working electrode surfaces were polished prior to each set of experiments and were periodically replaced on scanning > 0 V versus Fc to prevent the buildup of oxidized product on the electrode surfaces. Potentials were reported versus Fc, which was added as an internal standard for calibration at the end of each run. Solutions employed during CV studies were ~1 mM in analyte and 100 mM in [^{n}Pr$_4$N][BAr$^F{}_4$]. All data were collected in a positive-feedback IR compensation mode. The THF solution cell resistances were measured prior to each run to ensure resistances ≤ ~1000 Ω.

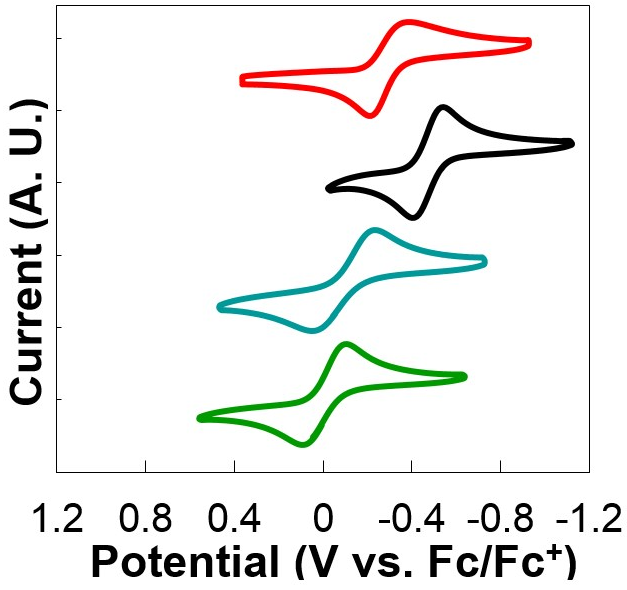

Figure S19. Isolated cerium(III/IV) redox couple (full scan) at 100 mV scan rates of **1-Cl** (red), **2-Cl** (black), **[3$^+$][BAr$^F{}_4$]** (cyan), **[4$^+$][BAr$^F{}_4$]** (green) in THF with 0.1 M [^{n}Pr$_4$N][BAr$^F{}_4$]; [analyte] = ca. 1 mM.

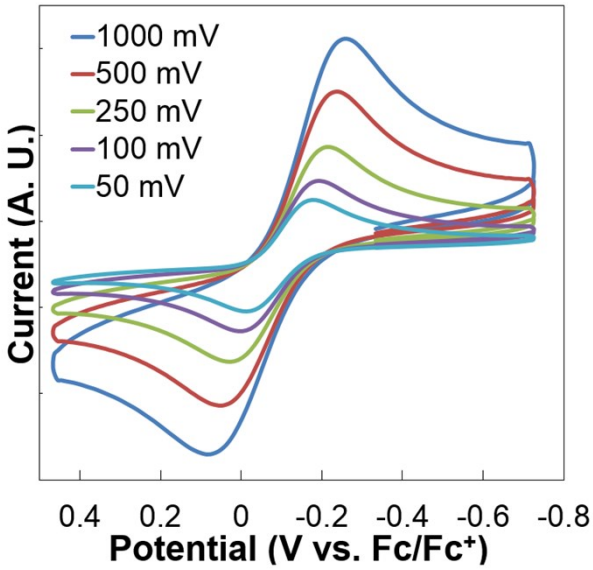

Figure S20. Isolated cerium(III/IV) redox couple at varying scan rates of **{[(Me$_3$Si)$_2$NC(N^{i}Pr)$_2$]$_2$Ce^{IV}[N(SiMe$_3$)$_2$]}[BAr$^F_4$] ([3$^+$][BAr$^F_4$])** in THF with 0.1 M [^{n}Pr$_4$N][BAr$^F_4$]; [analyte] = ca. 1 mM. $E_{1/2}$ of Ce^{III}/Ce^{IV} couple was determined to be −0.08 V vs. Fc/Fc$^+$.

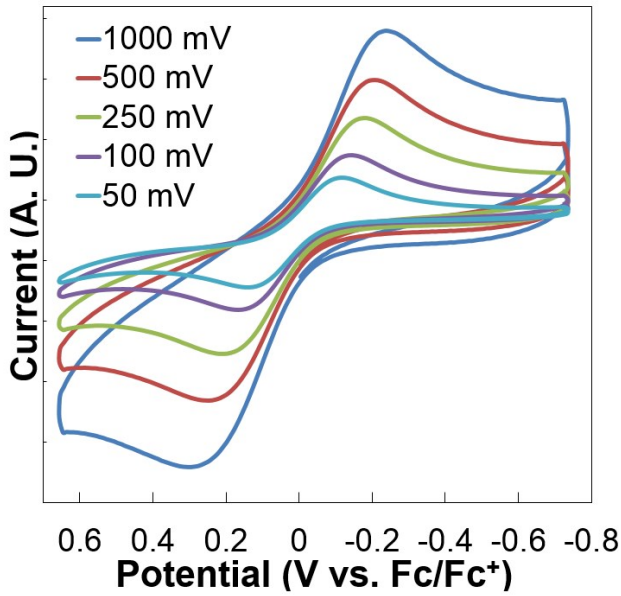

Figure S21. Isolated cerium(III/IV) redox couple at varying scan rates of **{[(Me$_3$Si)$_2$NC(N^{i}Pr)$_2$]$_3$Ce^{IV}} [BAr$^F_4$] ([4$^+$][BAr$^F_4$])** in THF with 0.1 M [^{n}Pr$_4$N][BAr$^F_4$]; [analyte] = ca. 1 mM. $E_{1/2}$ of Ce^{III}/Ce^{IV} couple was determined to be 0.01 V vs. Fc/Fc$^+$.

Table S5. Summary of $E_{1/2}$ of Ce^{III}/Ce^{IV} couple vs. Fc/Fc^{+} collected in THF

Compounds	**1-Cl**	**2-Cl**	**[3^{+}][BAr$^{F}_{4}$]**	**[4^{+}][BAr$^{F}_{4}$]**
$E_{1/2}$ (V)	−0.30	−0.46	−0.08	0.01

8. Magnetism

Magnetic data were collected on a Quantum Design Magnetic Property Measurement System (MPMS-7). Temperature-dependent data were collected under applied 0.5 T DC fields from 2 to 300 K, and field dependent data were performed at 2 K with varying applied magnetic field strengths ranging from 0 to 7 T. Corrections for the intrinsic diamagnetism of the samples were made using Pascal's constants.[16] For the measurements on **[4$^+$][BAr$^F_4$]**, diamagnetic contributions from quartz wool was accounted by using reported method.[17]

Each magnetism sample was prepared in the glovebox and placed in a heat-sealed compartment of a plastic drinking straw. The plastic drinking straws were evacuated overnight prior to use. These straws were then sealed at one end (~ 9.5 cm from the top) by heating a pair of forceps and crimping the sides of the straw until the two sides were fused together. Microcrystalline compound (30 ~ 40 mg) was loaded into the straw, capped with < 10 mg of quartz wool (dried at 250 ° C prior to use), and packed in tightly using a Q-tip. The other end of the plastic drinking straw was then sealed directly above the quartz wool, forming a small compartment (<1 cm). The sample and wool were massed four times each to the nearest 0.1 mg, and the values used were the averages of these mass measurements.

Fitting methods of the temperature independent paramagnetism (TIP) for **[4$^+$][BAr$^F_4$]**: the **4** data was used as a model of the J = 5/2 impurity contribution in order to remove the "Curie tails" in the **[4$^+$][BAr$^F_4$]** data. The TIP data of **[4$^+$][BAr$^F_4$]** was estimated by subtracting **4** data from the **[4$^+$][BAr$^F_4$]** data to a constant, χ_{TIP}, in the temperature range of 50−300 K. Two methods based on least squares were applied to fit the χ_{TIP} data which give consistent fitting results:

Method 1: subtract the χ of **4** data from the χ of **[4$^+$][BAr$^F_4$]** data to a constant use the following equation:

$$(\chi_{TIP})_T = (\chi_{[4]+})_T - k(\chi_4)_T$$

where subscript **4** and **[4⁺][BAr$^F_4$]** indicate $[(Me_3Si)_2NC(N^iPr)_2]_2Ce^{III}[N(SiMe_3)_2]$ and $\{[(Me_3Si)_2NC(N^iPr)_2]_2Ce^{IV}[N(SiMe_3)_2]\}[BAr^F{}_4]$, respectively. k is the percentage of the impurity present in the **[4⁺][BAr$^F_4$]** sample. Since χ_{TIP} is temperature independent, $(\chi_{TIP})_T$ versus T plot should be in a linear relationship with slope = 0 and intercept = χ_{TIP}. Based on least squares, the best fit by applying different k should minimize the sum of squared residual:

$$S = min\sum_{i=1}^{n}((\chi_{TIP})_T - \chi_{TIP})^2$$

where $(\chi_{TIP})_T$ is calculated from the experimental data by applying different k. χ_{TIP} is fitted by linear regression. The fitting outcome by method 1 from 2−300 K was shown in Figure S66.

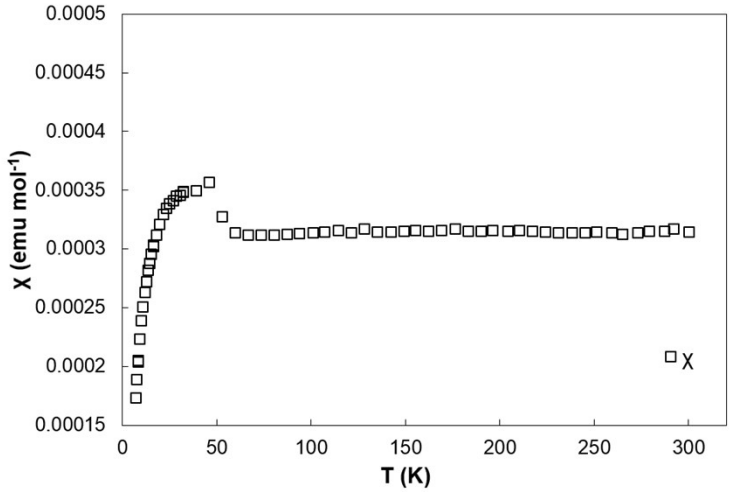

Figure S22. Fitting result of the χ_{TIP} data of **[4⁺][BAr$^F_4$]** by method 1. χ_{TIP} = 3.2 × 10^{-4} emu mol^{-1} with 1.2 % *J* = 5/2 impurity.

Method 2: subtract the χT of **4** data from the χT of **[4⁺][BAr$^F_4$]** data to a constant use the following equation:

$$(\chi T_{TIP})_T = (\chi T_{[4]^+})_T - k(\chi T_4)_T$$

Similarly, $(\chi T_{TIP})_T$ versus T plot should be in a linear relationship with slope = χ_{TIP} and intercept = 0. Based on least squares, the fitting outcome by method 2 from 2−300 K was shown in Figure S67.

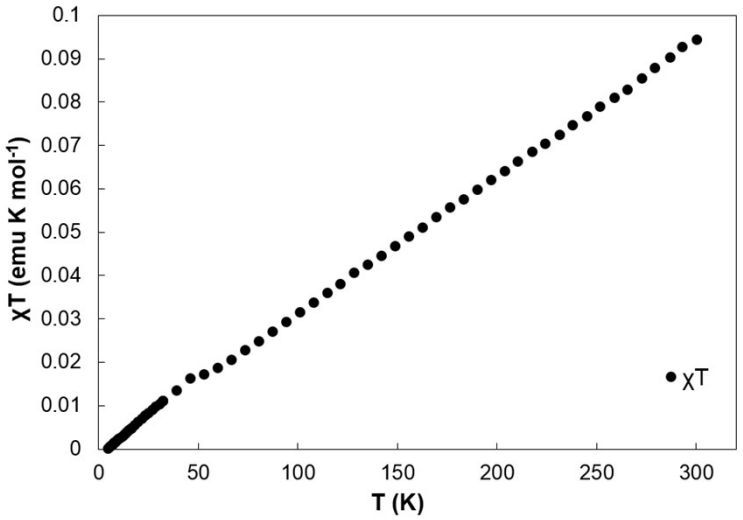

Figure S23. Fitting result of the χ_{TIP} data of **[4⁺][BAr$^{F}_{4}$]** by method 2. χ_{TIP} = 3.2 × 10^{-4} emu mol^{-1} with 1.2 % *J* = 5/2 impurity.

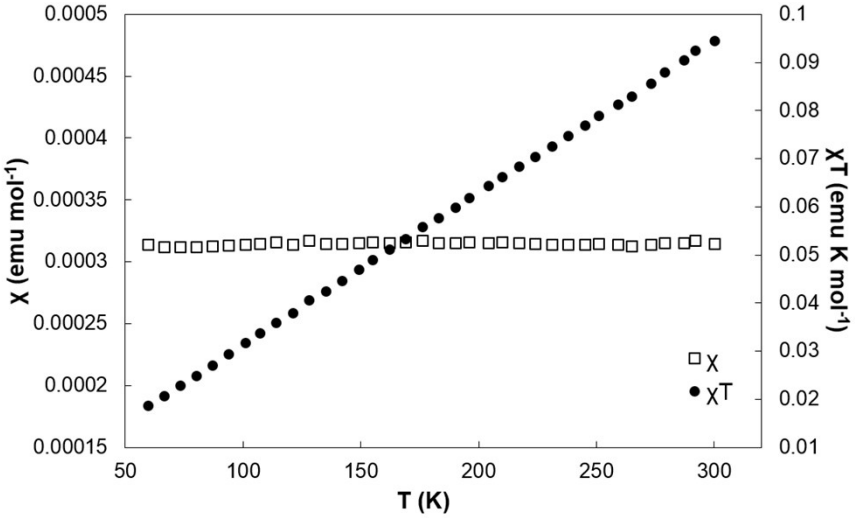

Figure S24. χ and χT versus T plots for **[4⁺][BAr$^{F}_{4}$]** fitted by method 1. χ_{TIP} = 3.2 × 10^{-4} emu mol^{-1} with 1.2 % *J* = 5/2 impurity.

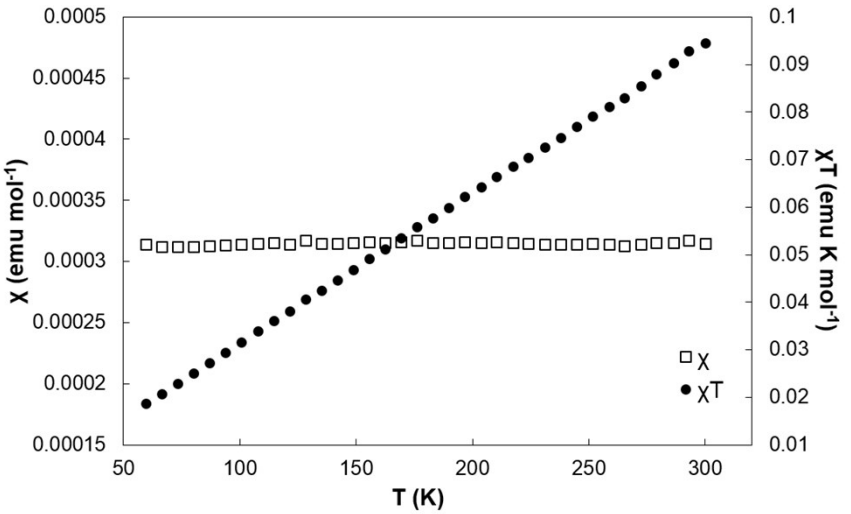

Figure S25. χ and χT versus T plots for **[4⁺][BAr$^{F}_{4}$]** fitted by method 2. χ_{TIP} = 3.2 × 10^{-4} emu mol^{-1} with 1.2 % *J* = 5/2 impurity.

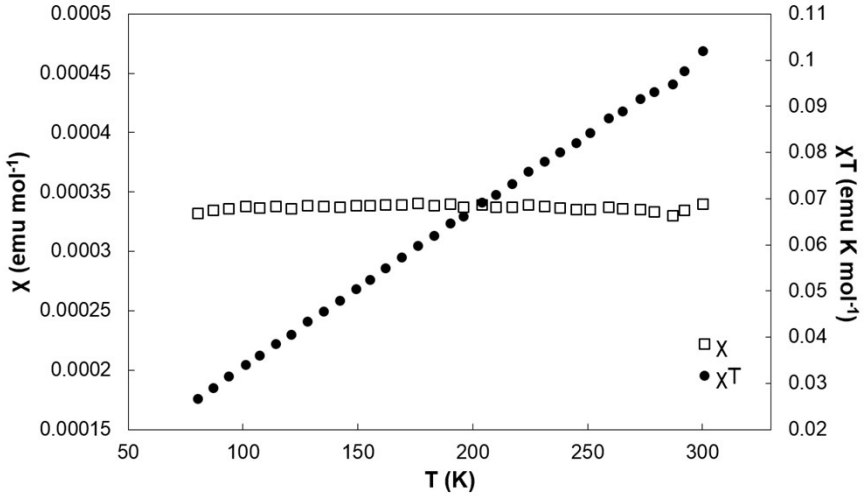

Figure S26. χ and χT versus T plots for **[4⁺][BAr$^{F}_{4}$]** (reproduced).

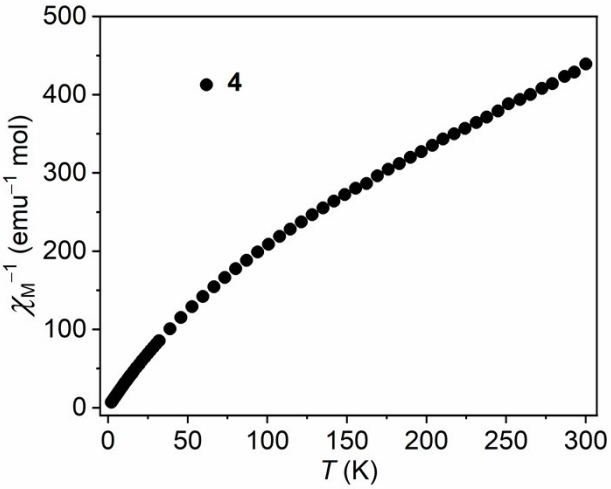

Figure S27. Inverse magnetic susceptibility as a function of temperature of temperature for complex at an applied field of 0.5 T.

9. Computational Details

Gaussian 09 Rev. A.02 was used in electronic structure calculations.[18] The B3LYP hybrid DFT method was employed with 28-electron small core pseudopotentials on cerium, with published segmented natural orbital basis sets incorporating quasi-relativistic effects,[19] and the 6-31G* basis set on all other atoms. All geometry optimizations were carried out starting from the coordinates of the crystal structures with the spin state restrained to singlet. Atomic orbital contributions to individual molecular orbitals were calculated with the AOMix program[20,21] through fragment molecular orbital analysis. Frequency calculations were performed to confirm that the optimized geometry was at the minimum (no imaginary frequencies). Calculated metal-ligand bond lengths were within 0.05 Å of the crystal structures in all cases. TD-DFT calculation was carried out for **1-Cl**, **2-Cl**, **[3$^+$]**, and **[4$^+$]** in gas phase. Molecular orbitals were rendered using Chemcraft v1.6 program.[22] For the LUMO energy correlation, the geometry optimizations and frequency calculations were performed with the conductor-like polarizable continuum model (CPCM)[23] with the Gaussian-defined solvent parameters for dichloromethane.

All-electron relativistic complete active space self-consistent field (CASSCF)[24-27] wave function calculations were performed, using the scalar relativistic Douglas-Kroll-Hess second order (DKH2) Hamiltonian.[28-30] Additionally, we performed Kohn-Sham (KS) density functional theory (DFT) calculations with the scalar all-electron zeroth-order regular approximation (ZORA) relativistic Hamiltonian.[31,32] The functionals used were the 'pure' (non-hybrid) functional PBE,[33] which has been reported to perform well with Lanthanide-containing molecules with slight difference to the PBE0 functional,[34] and the hybrid functional B3LYP,[35] to assess the impact of the KS delocalization error on ligand donation into the 4f shell.[36] The CASSCF and ZORA KS calculations were performed with the OpenMolcas[37] and Amsterdam Density Functional (ADF)[38] program packages, respectively. The geometries obtained by the Gaussian 09 calculations were used without further optimization. Due to the limitations of computing resources, the active spaces were chosen to include as many orbitals that have both 5d/4f contribution from Ce and 2s/2p contribution from N as possible. Accordingly, the active spaces were CAS(12,11) indicating 12 electrons in 11 active orbitals for **1-Cl** and **2-Cl**, and CAS(14,13) for **[3$^+$][BAr$^F_4$]** and **[4$^+$][BAr$^F_4$]**. The ANO-RCC-VTZP sets were used for Ce, N and Cl, the ANO-RCC-VDZP sets were used for Si and C, and the minimal basis ANO-RCC-MB was used for H.[39-41] For the KS-DFT calculations, the Slaster-type TZP basis sets were used for all complexes.[42] The electronic structures resulting from the spin-free CASSCF and KS-DFT calculations were subjected to natural bond orbital analyses using the NBO6.0 program package.[43]

Table S6. Cartesian coordinates of optimized structure for **1-Cl**

Ce	0.001399	0.001424	-0.23127	H	-1.83696	4.050442	-3.1577
Cl	0.003526	0.00062	-2.835	H	-0.521	2.866949	-3.07047
Si	-0.06479	3.107737	1.404835	H	-2.67477	0.595102	-2.05052
Si	-1.93844	2.800313	-1.00021	H	-3.81162	1.904623	-2.34868
Si	2.72266	-1.49423	1.408098	H	-3.78541	1.117961	-0.76642

Si	3.399054	0.272118	-1.00207	H	0.625115	-1.35985	2.833181
Si	-2.6589	-1.60766	1.404925	H	1.568631	-2.80661	3.153384
Si	-1.4622	-3.07667	-1.00168	H	0.524796	-2.7394	1.727649
N	-0.74613	2.094473	0.123394	H	4.785343	-0.38003	2.384018
N	2.188611	-0.4025	0.121458	H	3.939461	-1.38491	3.564945
N	-1.44395	-1.68829	0.119589	H	3.31484	0.220225	3.162428
C	1.268917	2.131437	2.342352	H	3.10977	-3.53268	-0.02293
C	-1.30983	3.625892	2.743005	H	3.914206	-3.68474	1.549131
C	0.741446	4.682731	0.719149	H	4.6335	-2.69008	0.277964
C	-3.03486	4.133787	-0.20244	H	5.05889	1.221498	0.658716
C	-1.08949	3.601228	-2.49094	H	5.75736	1.006401	-0.95083
C	-3.15072	1.465857	-1.58948	H	5.586061	-0.38381	0.122401
C	1.208843	-2.15389	2.347216	H	3.998724	-1.86366	-2.17839
C	3.794406	-0.67068	2.743202	H	4.422853	-0.45202	-3.15996
C	3.682342	-2.98654	0.734543	H	2.737098	-0.9893	-3.06623
C	5.101827	0.543829	-0.20091	H	1.872563	2.021191	-2.06317
C	3.659689	-0.86868	-2.48988	H	3.578318	2.333156	-2.35849
C	2.862975	1.991412	-1.59874	H	2.885603	2.721303	-0.78083
C	-2.48146	0.032168	2.350133	H	-1.50757	0.139403	2.847903
C	-2.48079	-2.951	2.736134	H	-3.23525	0.04534	3.148276
C	-4.42891	-1.69565	0.727464	H	-2.6413	0.919071	1.731603
C	-2.07893	-4.68914	-0.2025	H	-2.72422	-3.95349	2.375049
C	-2.57597	-2.73866	-2.49392	H	-3.17039	-2.722	3.559644
C	0.30034	-3.46787	-1.58362	H	-1.46875	-2.98183	3.15397
H	0.873026	1.238012	2.845125	H	-4.61598	-0.92481	-0.02792
H	1.667864	2.777088	3.135706	H	-5.15181	-1.55241	1.540895
H	2.10948	1.818887	1.717513	H	-4.64395	-2.66717	0.267637
H	-2.06273	4.33254	2.383928	H	-1.47348	-4.98944	0.659789
H	-0.76208	4.115395	3.559534	H	-1.99953	-5.48748	-0.95237
H	-1.83493	2.764555	3.170225	H	-3.12702	-4.6509	0.114844
H	1.495907	4.457206	-0.04254	H	-3.60724	-2.53351	-2.18443
H	1.234631	5.238472	1.527005	H	-2.59652	-3.61175	-3.15901
H	0.004166	5.354188	0.263939	H	-2.21938	-1.88253	-3.0749

H	-3.60515	3.753662	0.652487	H	0.817291	-2.62789	-2.05651
H	-3.75936	4.46713	-0.95736	H	0.251629	-4.27115	-2.33048
H	-2.48115	5.020037	0.125611	H	0.918176	-3.83179	-0.75446
H	-0.40117	4.396509	-2.18146				

Table S7. Comparison of parameters between X-ray structure and optimized model for **1-Cl**

	X-ray structure	**Optimized model**
Ce−N_{amide} (Å)	2.217(3)	2.251
Ce−Cl (Å)	2.597(2)	2.604

Table S8. Cartesian coordinates of optimized structure for **2-Cl**

Ce	0.836073	0.012772	-0.32198	H	3.740948	-3.36744	-3.20228
Si	1.469947	-3.0909	1.242468	H	2.294208	-4.02379	-2.42192
Si	-4.52772	1.249161	-0.65063	H	2.239716	-2.42787	-3.19658
Si	3.405517	-2.30353	-0.97157	H	-6.32337	1.345413	1.143626
C	4.611959	-3.54374	-0.1773	H	-6.22962	2.842529	0.214222
Cl	1.364989	0.225377	-2.88238	H	-5.02449	2.503886	1.463821
Si	-4.26083	-1.38031	1.023449	H	-3.11498	-1.48456	-1.8377
Si	1.864518	3.339841	-0.79641	H	-0.33158	-2.39542	-2.74797
Si	2.997502	1.967039	1.671392	H	-1.34766	-3.21896	-1.54701
C	4.474649	-0.77303	-1.30542	H	-1.87033	-3.12399	-3.23869
N	-1.42414	-0.53407	-1.05815	H	3.754553	0.377969	3.395433
C	-2.08409	0.006573	-0.02067	H	2.144845	-0.10302	2.8781
N	-3.51262	-0.03069	0.101945	H	3.544231	-0.50438	1.874553
C	-3.45507	2.609016	-1.40597	H	0.509678	-5.40056	1.165852
N	1.926684	1.907417	0.263419	H	1.667677	-5.17985	-0.15151
N	2.005673	-1.89216	0.06008	H	0.04488	-4.49875	-0.28821
C	0.051224	-2.37577	2.28551	H	-5.0496	0.028771	-2.79147
C	2.746656	-3.58014	2.564639	H	-6.43346	-0.06854	-1.69214
C	2.861362	-3.10216	-2.60105	H	-6.09464	1.432722	-2.55403
C	-5.62723	2.0461	0.670371	H	-1.16628	-0.16742	-3.79991

N	-1.26432	0.559888	0.891253	H	-2.71364	0.519552	-3.27923
C	-2.09006	-1.25497	-2.15185	H	-2.68885	-0.9807	-4.21978
C	-1.36411	-2.57818	-2.43361	H	5.414832	2.398822	2.107727
C	3.110311	0.268905	2.512821	H	5.193733	1.822132	0.446706
C	0.866478	-4.68702	0.411758	H	4.835981	3.504691	0.857805
C	-5.62722	0.581243	-2.04214	H	-0.00924	2.552432	-2.32348
C	-2.16755	-0.4143	-3.4381	H	-0.62701	3.565936	-0.99704
C	4.771789	2.472503	1.220943	H	0.212363	4.29748	-2.36785
C	0.200841	3.426366	-1.69926	H	1.186938	5.092015	0.905061
C	1.977844	4.985053	0.15424	H	1.853648	5.801005	-0.5703
C	2.404785	3.139887	3.046173	H	2.941493	5.140263	0.651094
C	3.265972	3.345416	-2.06997	H	3.068341	3.027388	3.914134
C	-4.33644	-1.03637	2.883924	H	1.388589	2.903357	3.380271
C	-6.04067	-1.69447	0.459177	H	2.421386	4.193675	2.754889
C	-3.33818	-3.0005	0.720071	H	3.209393	2.472927	-2.72814
C	-1.4788	2.835853	1.857732	H	4.251907	3.348664	-1.59199
C	-1.75242	1.333642	2.038965	H	3.198336	4.244251	-2.697
C	-1.11219	0.84917	3.348276	H	-4.89109	-1.84448	3.378563
H	4.175084	-4.53212	0.001104	H	-3.34831	-0.98559	3.350649
H	5.038848	-3.18476	0.765081	H	-4.85821	-0.09748	3.103537
H	5.443431	-3.68188	-0.88158	H	-6.42731	-2.52083	1.070301
H	4.983836	-0.44696	-0.39037	H	-6.72141	-0.84926	0.596994
H	3.926908	0.078301	-1.71801	H	-6.09436	-2.01144	-0.58712
H	5.252153	-1.04007	-2.03353	H	-3.69709	-3.75298	1.434031
H	-2.53104	2.241657	-1.85893	H	-2.25541	-2.92718	0.838726
H	-3.1859	3.377193	-0.67529	H	-3.53917	-3.38144	-0.28734
H	-4.03147	3.104383	-2.19739	H	-1.81882	3.394595	2.738224
H	-0.48433	-3.20767	2.761282	H	-0.40849	3.01836	1.724003
H	0.447255	-1.75	3.093455	H	-1.99967	3.232196	0.983457
H	-0.69308	-1.78067	1.749641	H	-2.83574	1.192132	2.118498
H	2.209826	-4.06641	3.390662	H	-1.49621	1.431365	4.193956
H	3.258529	-2.70465	2.979834	H	-1.32112	-0.20621	3.538325
H	3.508031	-4.27996	2.211641	H	-0.02402	0.977271	3.323707

Table S9. Comparison of parameters between X-ray structure and optimized model for **2-Cl**

	X-ray structure	**Optimized model**
Ce−N_{amide} (Å)	2.2432(17)	2.2654
Average Ce−$N_{guanidine}$ (Å)	2.4220(18)	2.4629
Ce−Cl (Å)	2.6062(6)	2.6231

Table S10. Cartesian coordinates of optimized gas phase structure for **[3$^+$]**

Ce	-0.00006	0.585973	0.000646	H	6.803214	-0.480622	-1.440822
Si	0.788941	3.712806	1.309218	H	7.215238	0.876559	-0.392496
C	2.446441	4.455086	0.779019	H	5.851354	1.008161	-1.504329
H	3.107176	3.717187	0.312813	C	6.332441	-1.392496	1.711482
H	2.967786	4.859783	1.655961	H	5.752646	-1.794294	2.549838
H	2.318462	5.276451	0.066844	H	7.129941	-0.767827	2.13392
C	-0.288524	5.114623	1.983164	H	6.819747	-2.231108	1.203931
H	-0.421599	5.928282	1.261819	C	2.617071	-3.516387	-1.63319
H	0.202987	5.544629	2.865517	H	1.68515	-3.457461	-1.063448
H	-1.282523	4.773333	2.292705	H	2.758507	-4.567703	-1.913219
C	1.098159	2.507246	2.737362	H	2.490518	-2.946531	-2.558407
H	0.168104	2.193569	3.226493	C	5.639121	-3.042493	-1.747393
H	1.699397	3.013465	3.503106	H	5.580823	-2.338533	-2.584791
H	1.661887	1.611887	2.455022	H	5.702529	-4.052797	-2.171556
Si	-0.78974	3.714254	-1.30986	H	6.580219	-2.861879	-1.217637
C	0.288447	5.116801	-1.981094	C	4.345145	-4.203732	0.7762
H	0.422533	5.928473	-1.257703	H	5.187018	-3.964391	1.432825
H	-0.203128	5.549517	-2.862078	H	4.546282	-5.190793	0.339116
H	1.282027	4.775504	-2.291974	H	3.451073	-4.305779	1.400539
C	-2.446836	4.456602	-0.778499	C	-2.576777	-0.685471	0.044592
H	-3.10962	3.71764	-0.316898	C	-2.872399	0.348807	2.27218
H	-2.966122	4.86649	-1.654245	H	-3.808015	-0.21705	2.220258
H	-2.31841	5.274241	-0.062141	C	-3.215088	1.846404	2.306343

C	-1.099206	2.510647	-2.739421	H	-2.305441	2.455698	2.346229
H	-0.169189	2.198131	-3.229322	H	-3.818653	2.079776	3.190732
H	-1.701268	3.017262	-3.504271	H	-3.780275	2.148505	1.419936
H	-1.661965	1.614587	-2.45747	C	-2.136638	-0.060384	3.555498
Si	5.279452	-0.320785	0.568099	H	-1.865669	-1.11996	3.544878
Si	4.115414	-2.964191	-0.634588	H	-2.773204	0.11932	4.428768
Si	-5.279988	-0.321598	-0.566951	H	-1.219453	0.523887	3.692871
Si	-4.114056	-2.965521	0.632704	C	-1.984106	-1.646362	-2.150428
N	-0.000454	2.795678	-0.000723	H	-3.00417	-2.026413	-2.048748
N	2.074237	0.020425	-1.080095	C	-1.888855	-0.91597	-3.495984
N	1.719289	-0.760564	1.001367	H	-2.605139	-0.093756	-3.568462
N	3.866138	-1.27184	-0.045469	H	-2.10469	-1.618902	-4.308183
N	-2.074965	0.020789	1.080236	H	-0.885323	-0.512665	-3.667345
N	-1.719109	-0.759855	-1.001166	C	-1.016005	-2.837479	-2.133071
N	-3.865901	-1.272446	0.04533	H	0.015559	-2.493334	-2.254635
C	2.576648	-0.685641	-0.044575	H	-1.239384	-3.526743	-2.955296
C	2.871366	0.349036	-2.272091	H	-1.080506	-3.396625	-1.194326
H	3.806671	-0.217445	-2.221093	C	-4.662993	1.161275	-1.556172
C	3.214921	1.846453	-2.305169	H	-3.919579	1.760232	-1.022365
H	2.305564	2.456268	-2.343331	H	-5.518021	1.817417	-1.761198
H	3.817571	2.080347	-3.190045	H	-4.236973	0.871281	-2.52119
H	3.781387	2.147342	-1.419174	C	-6.375856	0.319219	0.834161
C	2.134687	-0.058479	-3.555426	H	-6.79996	-0.483261	1.444805
H	1.862387	-1.117721	-3.545405	H	-7.21721	0.871848	0.395873
H	2.771199	0.120979	-4.428789	H	-5.851481	1.007866	1.504886
H	1.218215	0.527057	-3.692138	C	-6.332844	-1.392976	-1.710742
C	1.984794	-1.647464	2.150201	H	-5.753019	-1.793832	-2.549523
H	3.005345	-2.026296	2.048723	H	-7.130668	-0.768289	-2.132547
C	1.887994	-0.918056	3.49619	H	-6.819697	-2.23218	-1.203746
H	2.603366	-0.095146	3.569719	C	-5.63747	-3.045885	1.745763
H	2.104039	-1.621318	4.308044	H	-5.579575	-2.342551	2.583694
H	0.883923	-0.515914	3.667223	H	-5.699839	-4.056577	2.169176
C	1.018115	-2.83973	2.131678	H	-6.578871	-2.865734	1.216385
H	-0.013902	-2.49692	2.25326	C	-4.343372	-4.204021	-0.779102

H	1.242117	-3.529324	2.953457	H	-5.184485	-3.963751	-1.436357
H	1.083541	-3.398105	1.192541	H	-4.545594	-5.19117	-0.342727
C	4.661257	1.160997	1.558197	H	-3.448788	-4.306369	-1.402665
H	3.919147	1.761127	1.023886	C	-2.615096	-3.517953	1.630277
H	5.516227	1.816398	1.765785	H	-1.683275	-3.456598	1.060619
H	4.233284	0.869793	2.521982	H	-2.755183	-4.570074	1.907953
C	6.376027	0.32149	-0.831839	H	-2.489188	-2.95002	2.556755

Table S11. Comparison of parameters between X-ray structure and optimized gas phase model for **[3$^+$]**

	X-ray structure	**Optimized model**
Ce−N_{amide}	2.175(5)	2.20971
Average Ce−$N_{guanidine}$ (Å)	2.374(4)	2.40424
$N_{guanidine}$−Ce−$N_{guanidine}$ (°)	56.5(1), 56.3(1)	55.83513, 55.83302

Table S12. Cartesian coordinates of optimized gas phase structure for **[4$^+$]**

Ce	-0.008536	-0.003234	-0.00128	H	-1.6856	2.568892	2.520062
Si	3.593014	4.058103	-0.667333	H	-3.27616	2.628344	3.293225
Si	1.058902	5.317235	0.661935	H	-3.13501	2.826259	1.537977
Si	-5.354629	1.16624	-0.476169	C	-2.36094	0.047092	3.488463
Si	-5.141273	-1.821937	0.394627	H	-2.50052	-1.03431	3.413401
Si	1.690431	-5.213423	-0.332691	H	-2.90521	0.395857	4.373348
Si	4.173764	-3.49686	0.444622	H	-1.29821	0.247154	3.657578
N	1.277225	1.784097	1.05988	C	-6.71725	0.641586	-1.67629
N	0.660174	2.073037	-1.090008	H	-6.32176	0.142123	-2.56766
N	1.910634	3.878056	-0.027984	H	-7.243	1.54455	-2.0127
N	-2.143623	-0.518288	-1.083494	H	-7.46973	-0.0136	-1.22524
N	-2.203524	0.299533	1.014388	C	-6.18685	1.983238	1.014112
N	-4.336302	-0.261252	-0.036739	H	-6.85406	1.3089	1.55896
N	0.876892	-2.006789	1.089856	H	-6.80069	2.816383	0.646703
N	1.49439	-1.617469	-1.040703	H	-5.47345	2.401626	1.730685

N	2.411322	-3.599946	0.051474	C	-4.28873	2.462134	-1.3323
C	1.292081	2.598396	-0.018079	H	-3.39944	2.735159	-0.75739
C	1.999405	2.149183	2.294858	H	-4.88669	3.372864	-1.46206
H	2.359884	3.173474	2.180162	H	-3.96339	2.141704	-2.32656
C	1.076901	2.111738	3.518214	C	-5.82729	-2.75377	-1.10237
H	0.213426	2.770501	3.392696	H	-6.56731	-2.17333	-1.66082
H	1.623176	2.438621	4.409997	H	-6.33221	-3.65939	-0.74084
H	0.710717	1.098308	3.710719	H	-5.05308	-3.07513	-1.8058
C	3.22318	1.254024	2.525207	C	-6.57943	-1.50152	1.577226
H	2.933458	0.202625	2.577405	H	-6.26688	-0.95321	2.472598
H	3.711047	1.519309	3.470298	H	-6.97384	-2.47157	1.906473
H	3.961021	1.363141	1.72663	H	-7.41334	-0.95922	1.119741
C	0.474531	2.868411	-2.319362	C	-3.90149	-2.93717	1.272041
H	0.945102	3.841836	-2.157008	H	-2.95024	-3.02759	0.739715
C	-1.01097	3.107234	-2.60534	H	-4.32855	-3.94445	1.352979
H	-1.531014	2.162692	-2.775602	H	-3.68925	-2.59153	2.288484
H	-1.128743	3.725205	-3.503046	C	1.606674	-2.42758	0.034027
H	-1.499952	3.618199	-1.774117	C	0.826527	-2.79648	2.33441
C	1.150573	2.215906	-3.532076	H	1.563536	-3.59987	2.247674
H	2.22532	2.088826	-3.377518	C	1.195686	-1.957	3.562763
H	1.010334	2.842557	-4.420184	H	2.206508	-1.54908	3.485347
H	0.717047	1.233675	-3.75024	H	1.152278	-2.57729	4.465009
C	4.658052	4.929106	0.628647	H	0.497243	-1.12546	3.702102
H	4.326831	5.948271	0.854038	C	-0.55479	-3.43526	2.528395
H	5.686634	5.002873	0.253103	H	-1.32342	-2.66742	2.644146
H	4.691859	4.370591	1.571239	H	-0.56285	-4.05906	3.429773
C	3.675977	5.033897	-2.28493	H	-0.83358	-4.06433	1.678628
H	3.018198	4.618727	-3.056634	C	2.269793	-1.87171	-2.26811
H	4.703042	4.973526	-2.668943	H	2.76147	-2.84216	-2.15797
H	3.434456	6.093774	-2.171079	C	3.351464	-0.80156	-2.45692
C	4.337465	2.357918	-1.023879	H	2.895116	0.184437	-2.56897
H	3.974845	1.56083	-0.370589	H	3.943536	-1.00779	-3.35618
H	5.42546	2.41977	-0.895912	H	4.032115	-0.76219	-1.6024
H	4.153775	2.051135	-2.057689	C	1.373605	-1.94715	-3.50973

C	1.539734	5.683706	2.456227	H	0.638438	-2.75187	-3.42969
H	1.13249	4.958958	3.168398	H	1.984804	-2.13814	-4.39894
H	1.133103	6.666545	2.728697	H	0.837098	-1.00704	-3.67557
H	2.623399	5.729093	2.60545	C	1.434635	-6.30081	1.193811
C	1.463903	6.856728	-0.355154	H	2.360328	-6.50109	1.740965
H	2.50566	7.18298	-0.275171	H	1.039429	-7.26985	0.861451
H	0.843708	7.677221	0.028908	H	0.711049	-5.88204	1.899913
H	1.223421	6.735054	-1.416547	C	2.808066	-6.15334	-1.53228
C	-0.807407	5.05725	0.584802	H	3.024304	-5.57759	-2.43886
H	-1.198298	5.254137	-0.418491	H	2.285593	-7.06789	-1.84141
H	-1.291034	5.765293	1.269168	H	3.760993	-6.46553	-1.09273
H	-1.119215	4.052918	0.882343	C	0.017275	-4.9719	-1.16522
C	-2.91745	-0.160766	-0.037101	H	-0.64044	-4.28715	-0.62246
C	-2.736688	-1.111214	-2.29688	H	-0.49036	-5.94323	-1.21503
H	-3.824465	-1.049013	-2.202979	H	0.117784	-4.60406	-2.19081
C	-2.346496	-0.346837	-3.567967	C	4.537426	-1.83758	1.259093
H	-2.729785	0.676344	-3.553642	H	4.140287	-0.98486	0.700928
H	-2.768395	-0.84765	-4.446516	H	5.625218	-1.70953	1.321563
H	-1.260369	-0.306154	-3.701481	H	4.14472	-1.78815	2.279115
C	-2.351414	-2.590088	-2.421106	C	4.64544	-4.86139	1.664096
H	-1.269419	-2.698718	-2.519705	H	4.028608	-4.84352	2.569419
H	-2.819547	-3.035815	-3.30643	H	5.686028	-4.69806	1.97315
H	-2.667827	-3.16308	-1.545186	H	4.596073	-5.86909	1.23862
C	-2.877408	0.76908	2.238315	C	5.291703	-3.66575	-1.07264
H	-3.941707	0.536541	2.141178	H	5.141442	-4.60249	-1.61708
C	-2.735837	2.288407	2.402107	H	6.3355	-3.65369	-0.7318
				H	5.174921	-2.84186	-1.78332

Table S13. Comparison of parameters between X-ray structure and optimized gas phase model for **[4^{+}]**

	X-ray structure	**Optimized model**
Average Ce−$N_{guanidine}$ (Å)	2.398	2.44234

Average $N_{guanidine}$−Ce−$N_{guanidine}$ (°)	55.71	54.94389

Table S14. The major orbital contributions of the lowest energy vertical excitation for **1-Cl**

	Energy (eV)	Osc. Strength	Contributions
1-Cl	2.11	0.0017	HOMO-2 → LUMO+5 (14%) HOMO-1 → LUMO+6 (68%) HOMO-2 → LUMO+4 (3%) HOMO-1 → LUMO+3 (3%) HOMO → LUMO+3 (2%)
	2.12	0.0023	HOMO-2 → LUMO+6 (65%) HOMO-1 → LUMO+5 (16%) HOMO-2 → LUMO+3 (3%) HOMO-1 → LUMO+4 (3%) HOMO → LUMO+4 (3%)
	2.21	0.041	HOMO-2 → LUMO+6 (26%) HOMO-1 → LUMO+5 (43%) HOMO-2 → LUMO+4 (2%) HOMO-2 → LUMO+5 (2%) HOMO-1 → LUMO+2 (9%) HOMO-1 → LUMO+3 (2%) HOMO-1 → LUMO+6 (4%) HOMO → LUMO (3%)
	2.22	0.0414	HOMO-2 → LUMO+5 (46%) HOMO-1 → LUMO+6 (22%) HOMO-2 → LUMO+2 (9%) HOMO-2 → LUMO+3 (3%) HOMO-2 → LUMO+6 (4%) HOMO-1 → LUMO+4 (2%) HOMO → LUMO+1 (3%)
	2.46	0.0012	HOMO-2 → LUMO+1 (13%) HOMO-1 → LUMO (13%) HOMO → LUMO+2 (10%)

			HOMO → LUMO+5 (24%) HOMO-5 → LUMO+6 (8%) HOMO-4 → LUMO+1 (3%) HOMO-4 → LUMO+3 (2%) HOMO-4 → LUMO+4 (4%) HOMO-3 → LUMO (3%) HOMO-3 → LUMO+1 (2%) HOMO-3 → LUMO+3 (4%) HOMO-3 → LUMO+4 (2%)

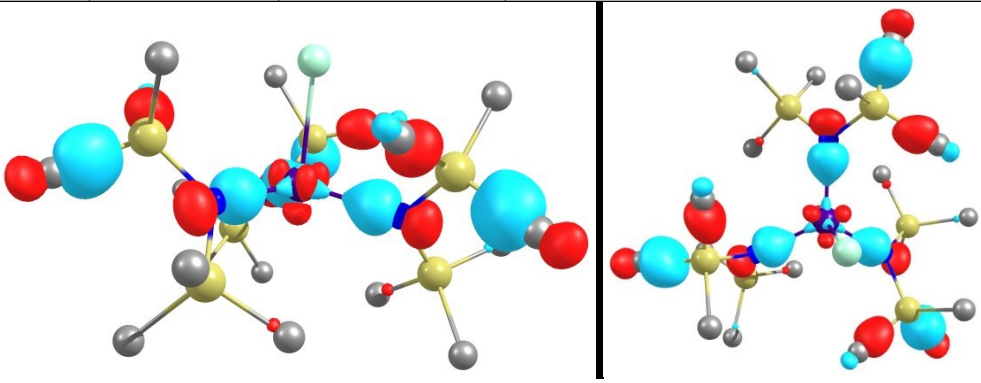

Figure S28. Calculated HOMO-5 of ground state geometry of **1-Cl** (gas phase) viewed from two orientations (rendered at contour value of 0.05).

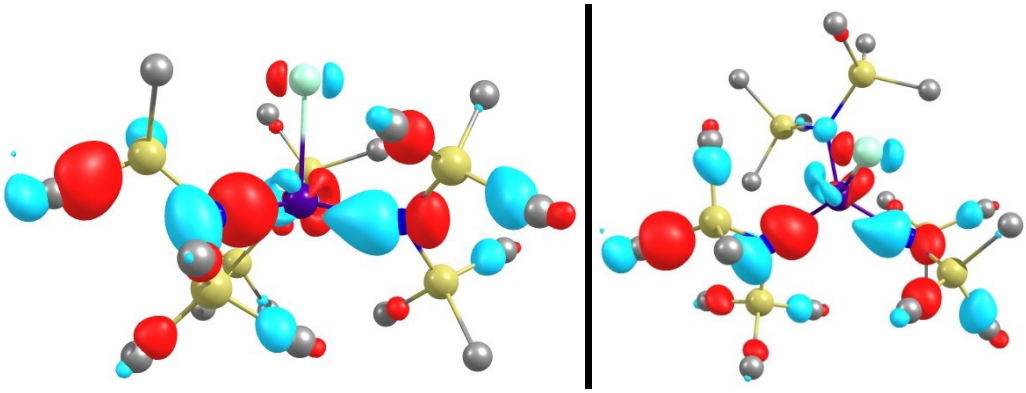

Figure S29. Calculated HOMO-4 of ground state geometry of **1-Cl** (gas phase) viewed from two orientations (rendered at contour value of 0.05).

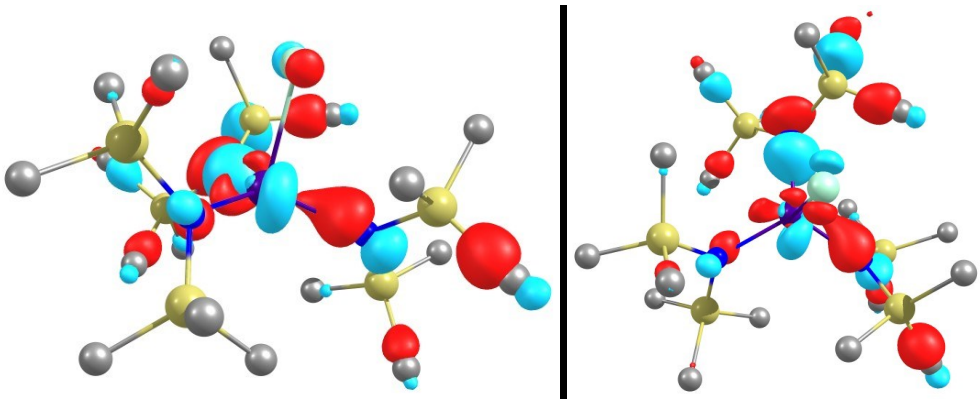

Figure S30. Calculated HOMO-3 of ground state geometry of **1-Cl** (gas phase) viewed from two orientations (rendered at contour value of 0.05).

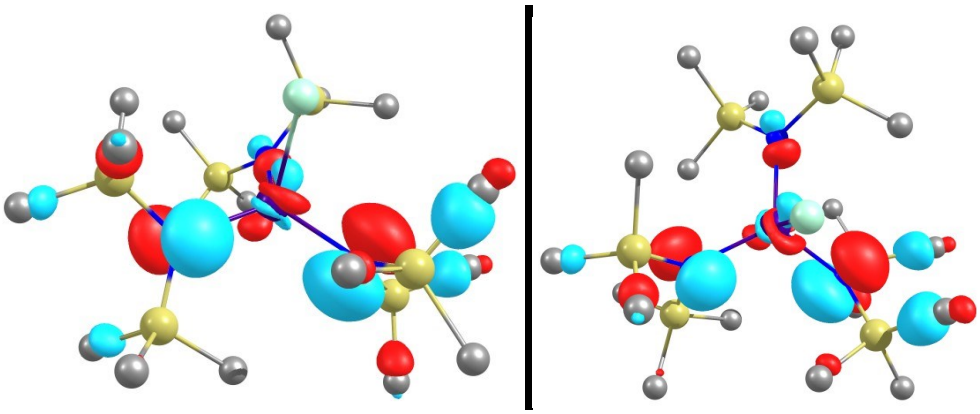

Figure S31. Calculated HOMO-2 of ground state geometry of **1-Cl** (gas phase) viewed from two orientations (rendered at contour value of 0.05).

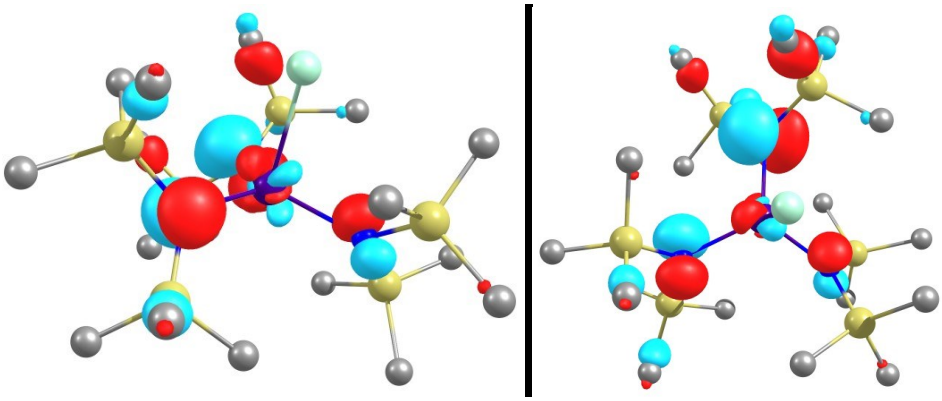

Figure S32. Calculated HOMO-1 of ground state geometry of **1-Cl** (gas phase) viewed from two orientations (rendered at contour value of 0.05).

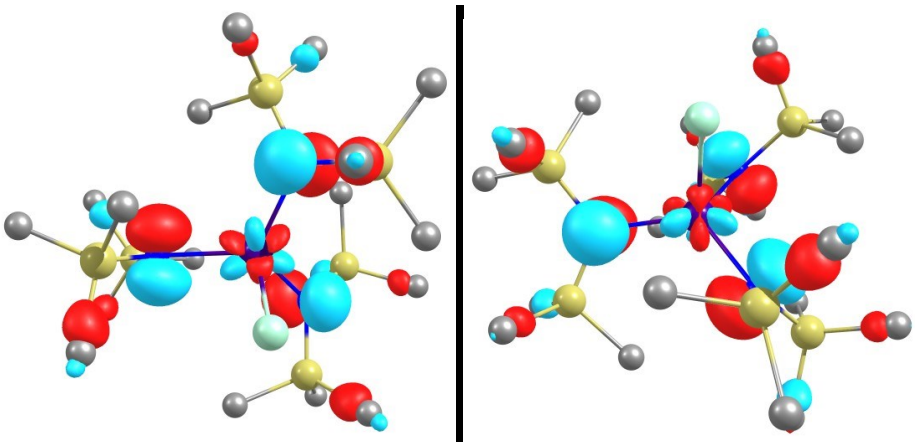

Figure S33. Calculated HOMO of ground state geometry of **1-Cl** (gas phase) viewed from two orientations (rendered at contour value of 0.05).

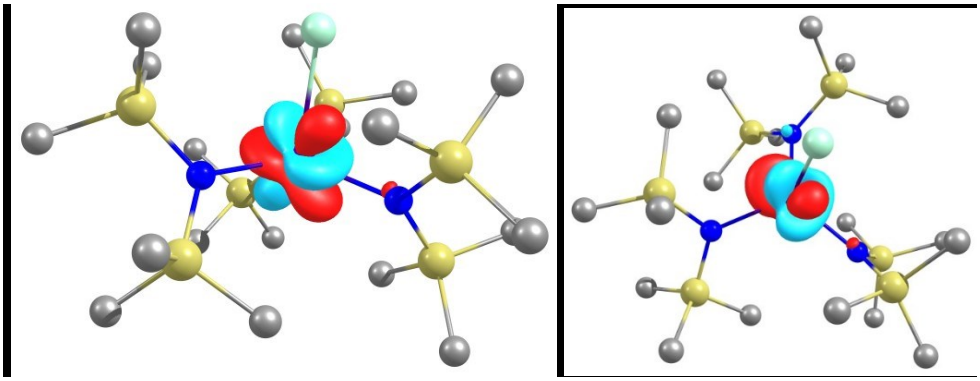

Figure S34. Calculated LUMO of ground state geometry of **1-Cl** (gas phase) viewed from two orientations (rendered at contour value of 0.05).

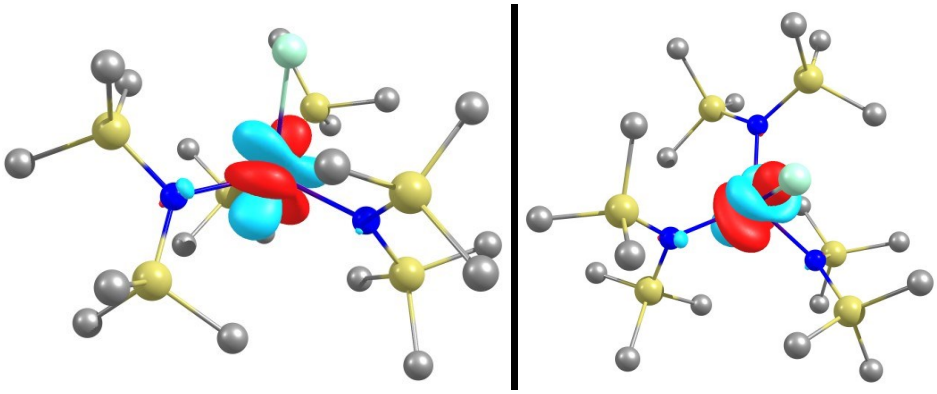

Figure S35. Calculated LUMO+1 of ground state geometry of **1-Cl** (gas phase) viewed from two

orientations (rendered at contour value of 0.05).

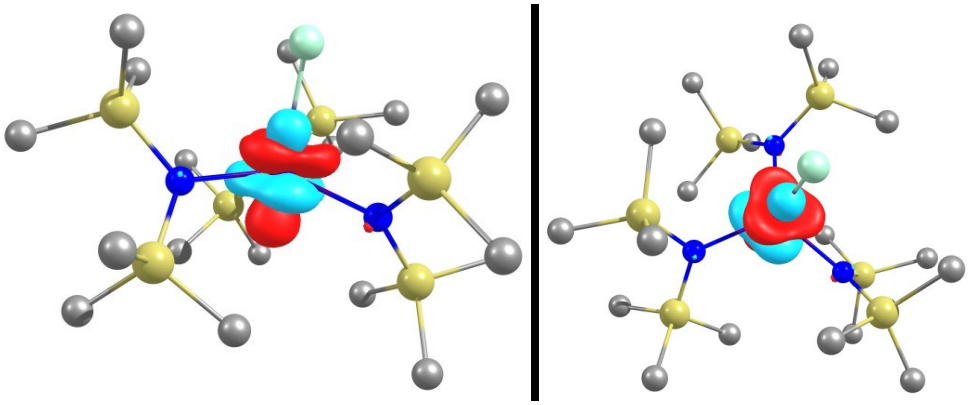

Figure S36. Calculated LUMO+2 of ground state geometry of **1-Cl** (gas phase) viewed from two orientations (rendered at contour value of 0.05).

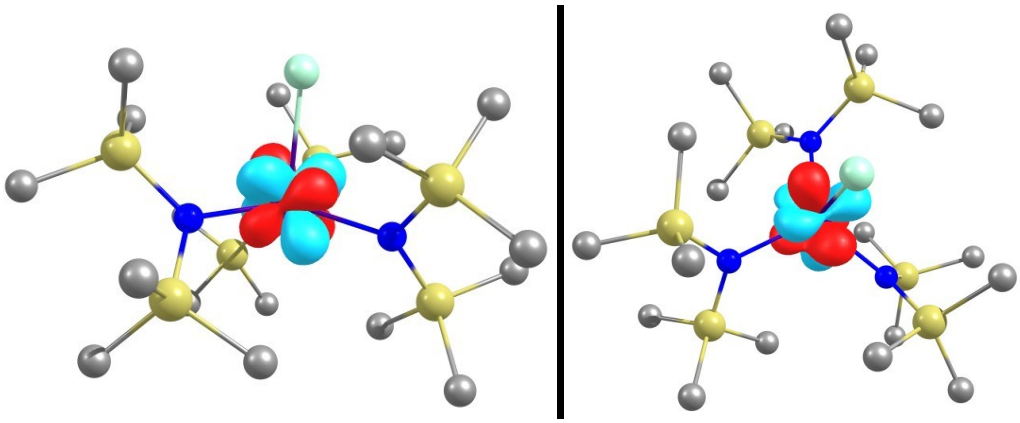

Figure S37. Calculated LUMO+3 of ground state geometry of **1-Cl** (gas phase) viewed from two orientations (rendered at contour value of 0.05).

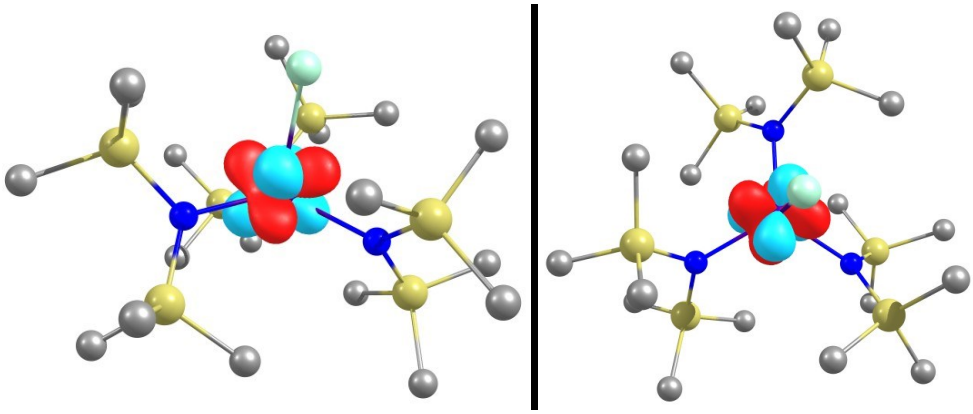

Figure S38. Calculated LUMO+4 of ground state geometry of **1-Cl** (gas phase) viewed from two

orientations (rendered at contour value of 0.05).

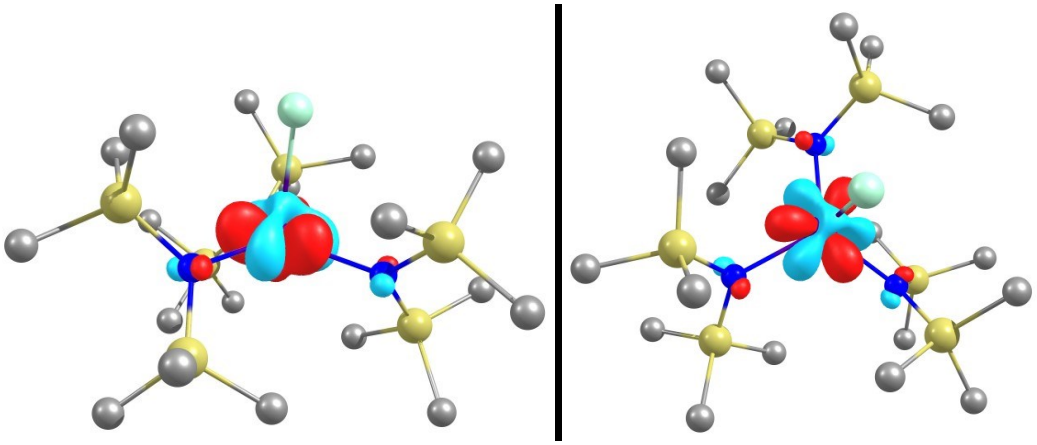

Figure S39. Calculated LUMO+5 of ground state geometry of **1-Cl** (gas phase) viewed from two orientations (rendered at contour value of 0.05).

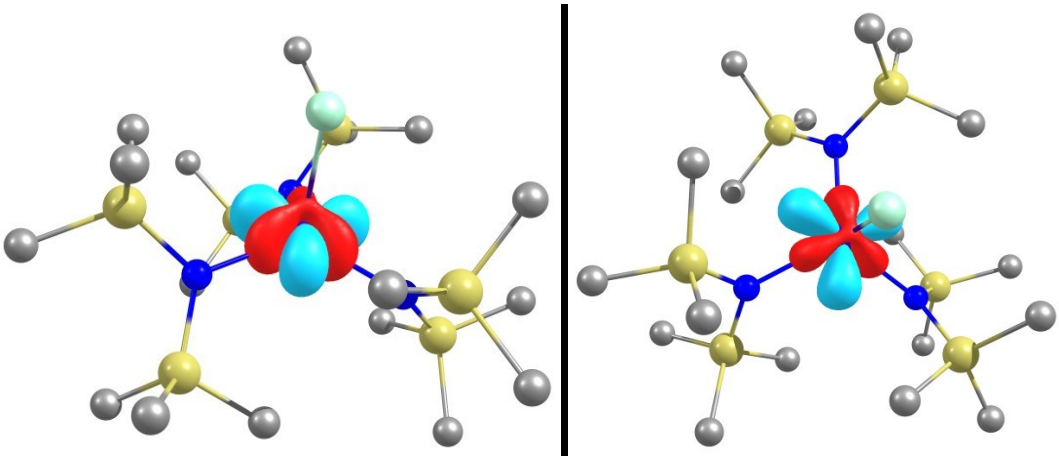

Figure S40. Calculated LUMO+6 of ground state geometry of **1-Cl** (gas phase) viewed from two orientations (rendered at contour value of 0.05).

Table S15. The major orbital contributions of the lowest energy vertical excitation for **2-Cl**

	Energy (eV)	Osc. Strength	Contributions
2-Cl	1.74	0.0241	HOMO-1 → LUMO (13%) HOMO-1 → LUMO+2 (10%) HOMO → LUMO (12%) HOMO → LUMO+4 (15%)

			HOMO → LUMO+6 (26%) HOMO-1 → LUMO+5 (4%) HOMO → LUMO+2 (2%) HOMO → LUMO+3 (8%)
	1.76	0.0065	HOMO-1 → LUMO (78%) HOMO → LUMO (5%) HOMO → LUMO+4 (5%) HOMO → LUMO+6 (5%)
	1.90	0.0037	HOMO-2 → LUMO (20%) HOMO-2 → LUMO+2 (17%) HOMO-1 → LUMO+2 (19%) HOMO-1 → LUMO+5 (13%) HOMO-2 → LUMO+1 (7%) HOMO-1 → LUMO+1 (6%) HOMO-1 → LUMO+3 (7%) HOMO-1 → LUMO+4 (4%)
	1.91	0.0032	HOMO-2 → LUMO (56%) HOMO-2 → LUMO+1 (22%) HOMO-2 → LUMO+4 (4%) HOMO-1 → LUMO+1 (2%) HOMO-1 → LUMO+2 (4%) HOMO-1 → LUMO+4 (2%)
	2.02	0.0031	HOMO-2 → LUMO+3 (64%) HOMO-2 → LUMO+2 (5%) HOMO-2 → LUMO+4 (3%) HOMO-2 → LUMO+5 (7%) HOMO-2 → LUMO+6 (9%) HOMO-1 → LUMO+1 (2%) HOMO-1 → LUMO+2 (3%)
	2.16	0.0209	HOMO-2 → LUMO+5 (42%) HOMO-1 → LUMO+5 (21%) HOMO-4 → LUMO+5 (2%) HOMO-1 → LUMO+1 (6%)

			HOMO-1 → LUMO+2 (9%) HOMO-1 → LUMO+3 (3%) HOMO-1 → LUMO+6 (3%)

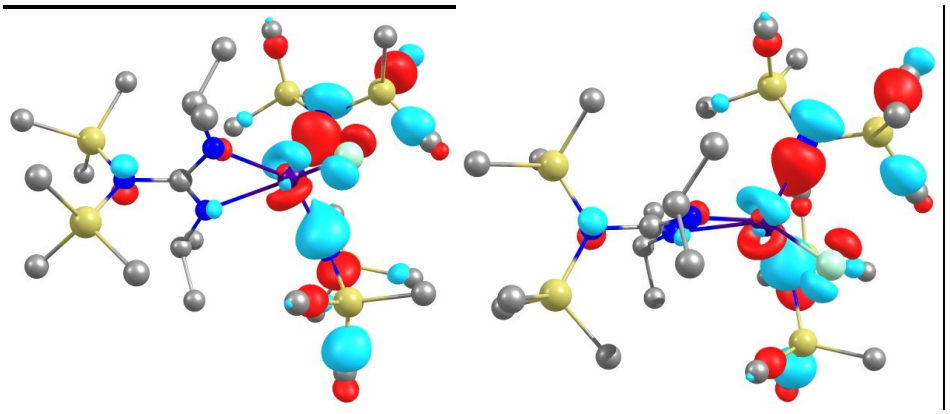

Figure S41. Calculated HOMO-4 of ground state geometry of **2-Cl** (gas phase) viewed from two orientations (rendered at contour value of 0.05).

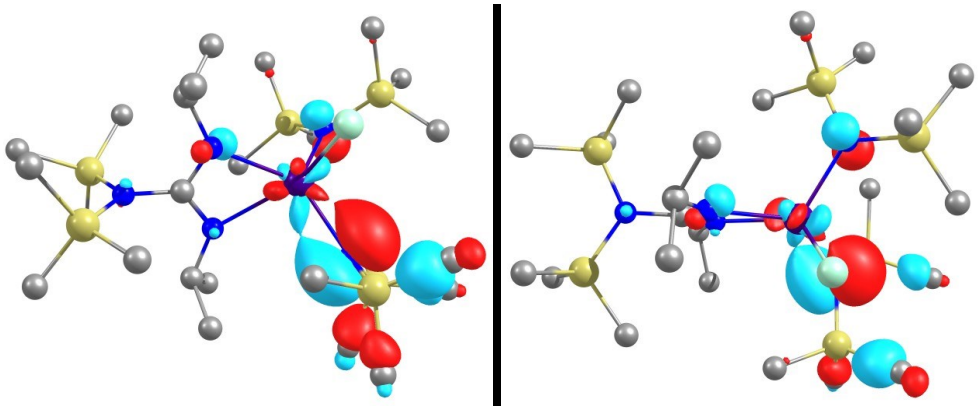

Figure S42. Calculated HOMO-2 of ground state geometry of **2-Cl** (gas phase) viewed from two orientations (rendered at contour value of 0.05).

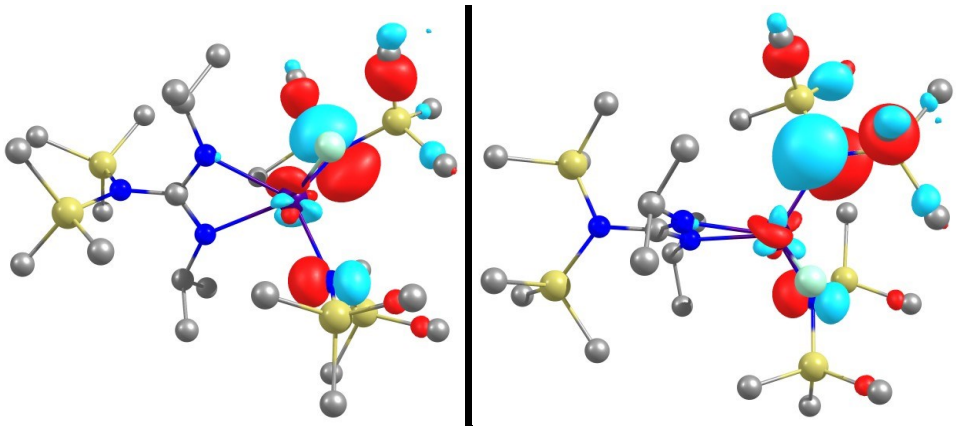

Figure S43. Calculated HOMO-1 of ground state geometry of **2-Cl** (gas phase) viewed from two orientations (rendered at contour value of 0.05).

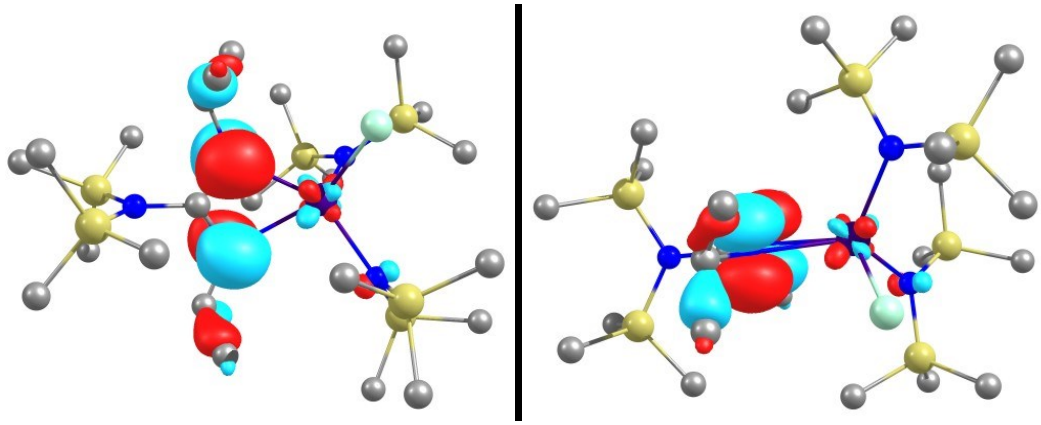

Figure S44. Calculated HOMO of ground state geometry of **2-Cl** (gas phase) viewed from two orientations (rendered at contour value of 0.05).

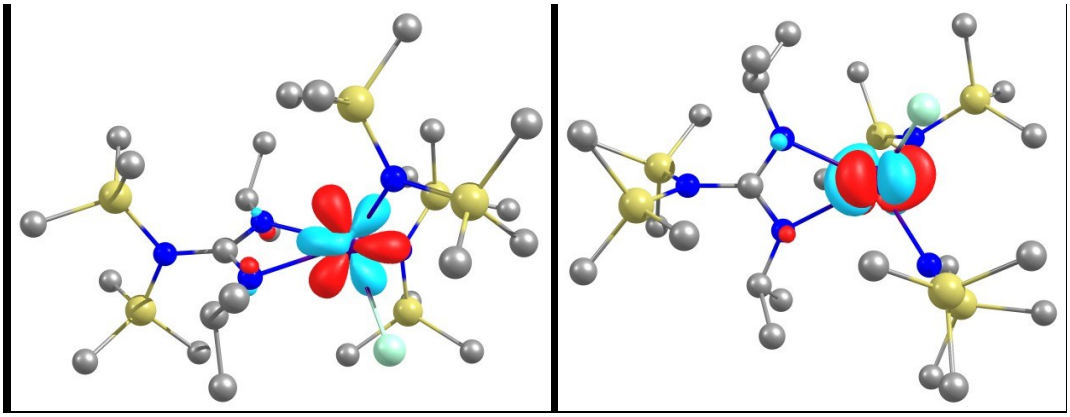

Figure S45. Calculated LUMO of ground state geometry of **2-Cl** (gas phase) viewed from two orientations (rendered at contour value of 0.05).

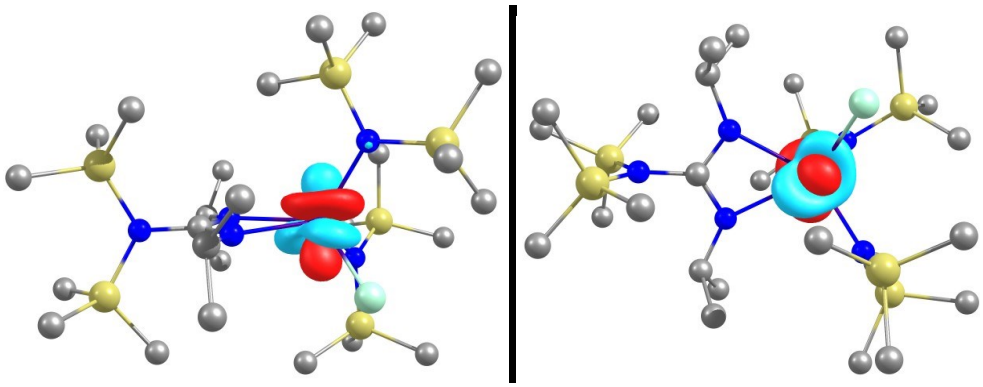

Figure S46. Calculated LUMO+1 of ground state geometry of **2-Cl** (gas phase) viewed from two orientations (rendered at contour value of 0.05).

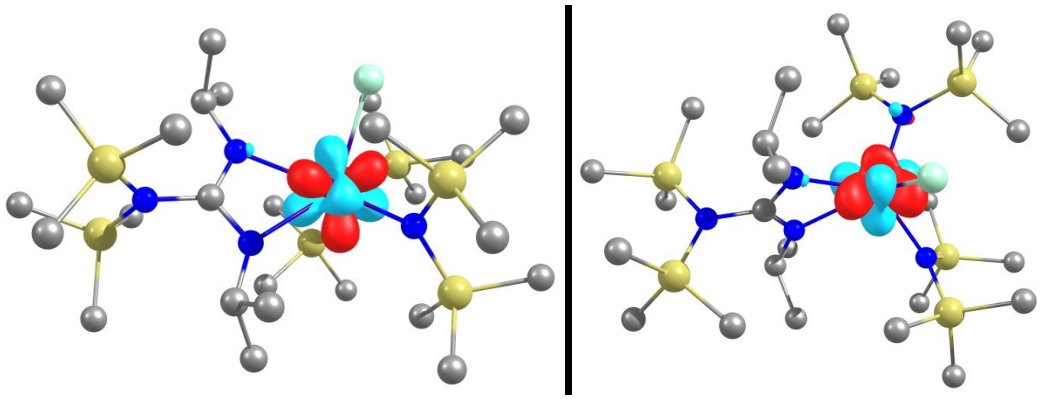

Figure S47. Calculated LUMO+2 of ground state geometry of **2-Cl** (gas phase) viewed from two orientations (rendered at contour value of 0.05).

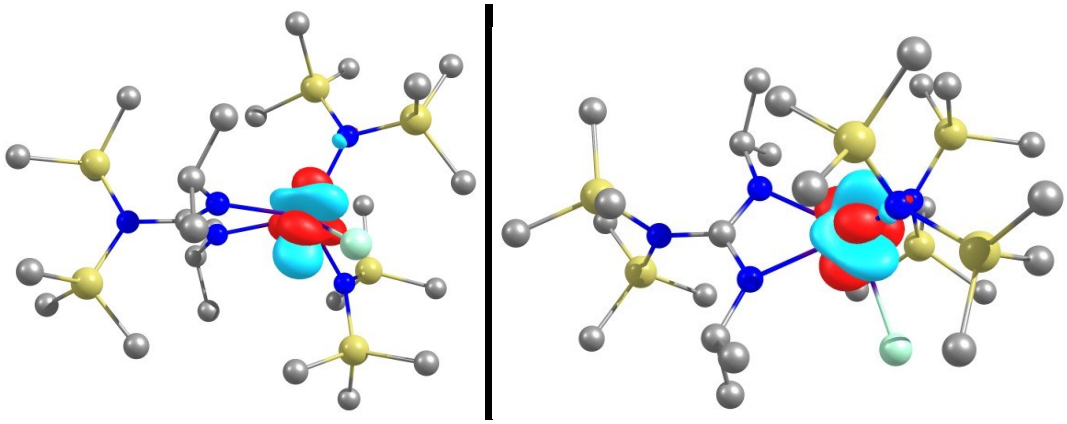

Figure S48. Calculated LUMO+3 of ground state geometry of **2-Cl** (gas phase) viewed from two orientations (rendered at contour value of 0.05).

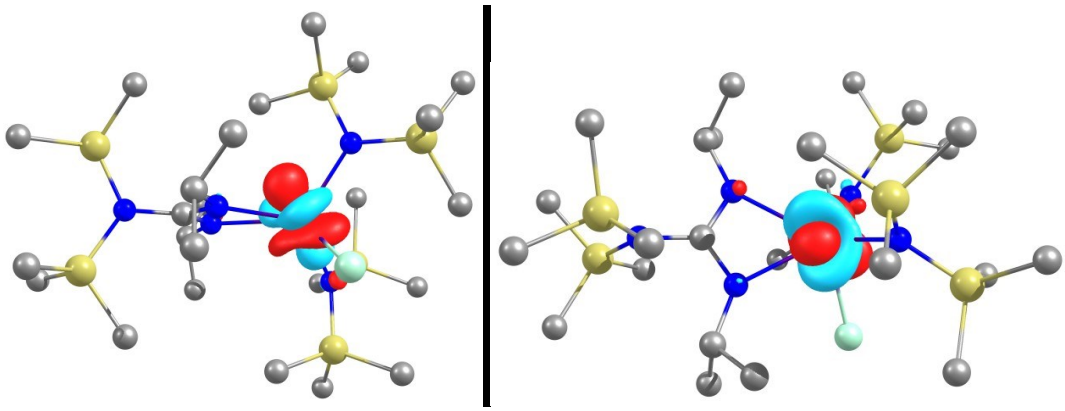

Figure S49. Calculated LUMO+4 of ground state geometry of **2-Cl** (gas phase) viewed from two orientations (rendered at contour value of 0.05).

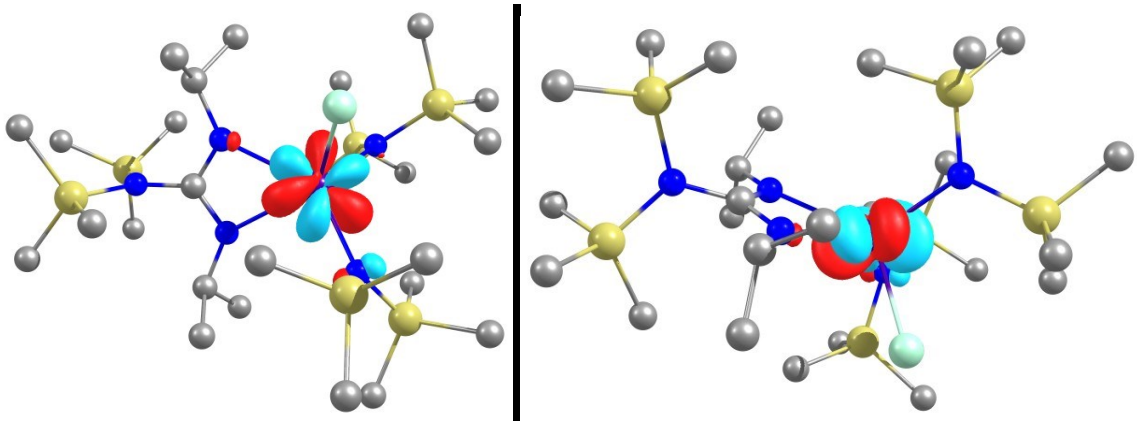

Figure S50. Calculated LUMO+5 of ground state geometry of **2-Cl** (gas phase) viewed from two orientations (rendered at contour value of 0.05).

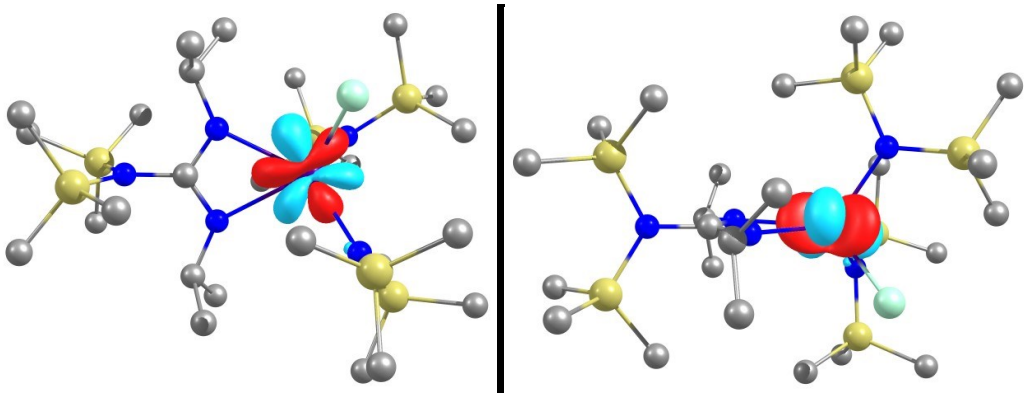

Figure S51. Calculated LUMO+6 of ground state geometry of **2-Cl** (gas phase) viewed from two orientations (rendered at contour value of 0.05).

Table S16. The major orbital contributions of the lowest energy vertical excitation for **[3$^+$]**

	Energy (eV)	Osc. Strength	Contributions
[3$^+$]	1.63	0.0023	HOMO-1 → LUMO+6 (73%) HOMO → LUMO+5 (16%) HOMO-1 → LUMO (2%) HOMO-1 → LUMO+4 (4%)
	1.66	0.0095	HOMO-1 → LUMO+5 (41%) HOMO → LUMO+6 (40%) HOMO → LUMO (8%) HOMO → LUMO+4 (8%)
	1.72	0.0304	HOMO-1 → LUMO+5 (24%) HOMO → LUMO (18%) HOMO → LUMO+6 (46%) HOMO-1 → LUMO+1 (5%)
	1.97	0.0031	HOMO-4 → LUMO+1 (82%) HOMO-2 → LUMO+1 (14%)
	1.98	0.0094	HOMO-4 → LUMO (14%) HOMO-4 → LUMO+2 (46%) HOMO-2 → LUMO+2 (11%) HOMO → LUMO+5 (11%) HOMO-1 → LUMO (3%) HOMO-1 → LUMO+6 (6%) HOMO → LUMO+1 (2%)
	2.09	0.0025	HOMO-4 → LUMO+2 (19%) HOMO-4 → LUMO+4 (48%) HOMO-4 → LUMO (7%) HOMO-2 → LUMO+4 (7%) HOMO → LUMO+1 (4%) HOMO → LUMO+5 (4%)

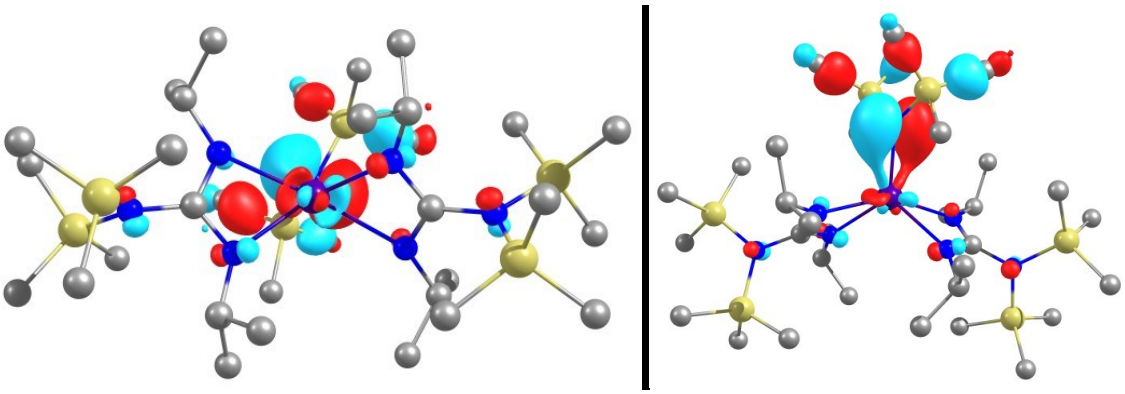

Figure S52. Calculated HOMO-4 of ground state geometry of **[3$^+$]** (gas phase) viewed from two orientations (rendered at contour value of 0.05).

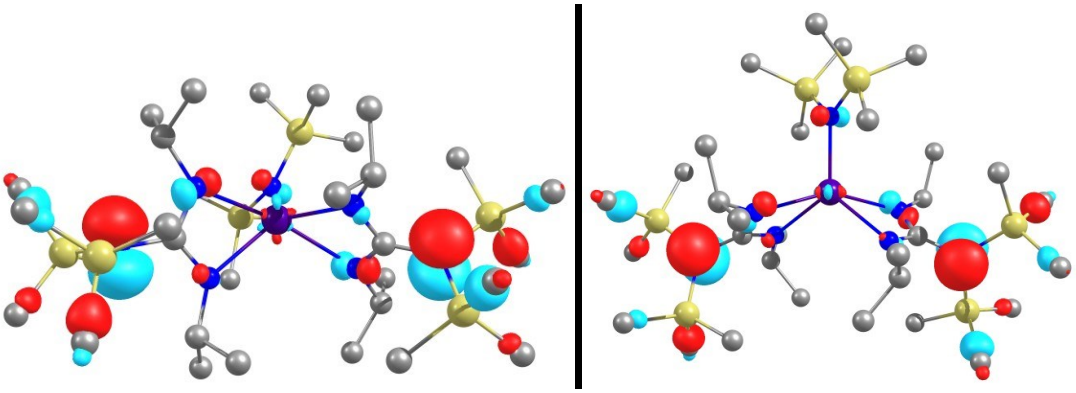

Figure S53. Calculated HOMO-2 of ground state geometry of **[3$^+$]** (gas phase) viewed from two orientations (rendered at contour value of 0.05).

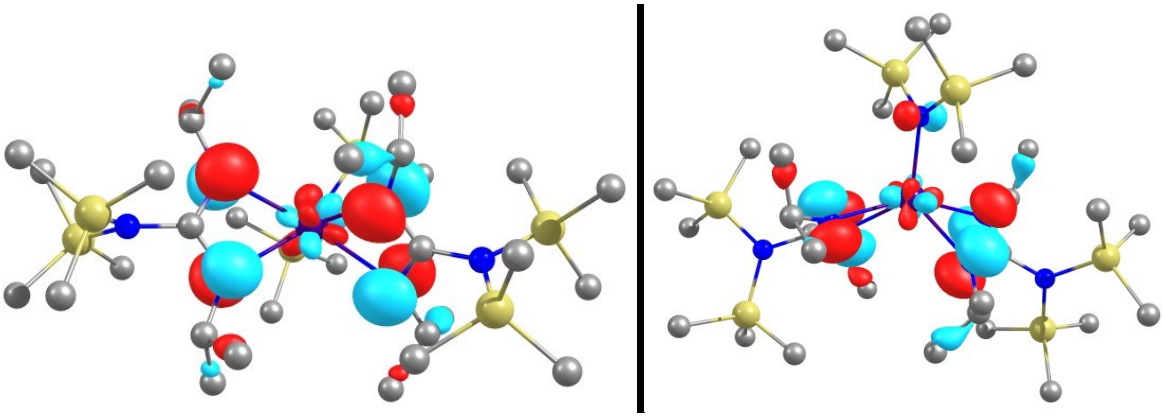

Figure S54. Calculated HOMO-1 of ground state geometry of **[3$^+$]** (gas phase) viewed from two orientations (rendered at contour value of 0.05).

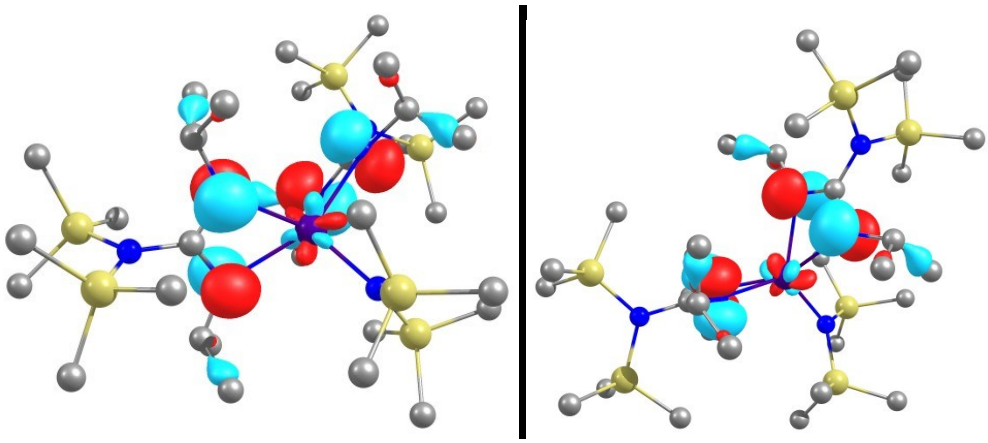

Figure S55. Calculated HOMO of ground state geometry of **[3$^+$]** (gas phase) viewed from two orientations (rendered at contour value of 0.05).

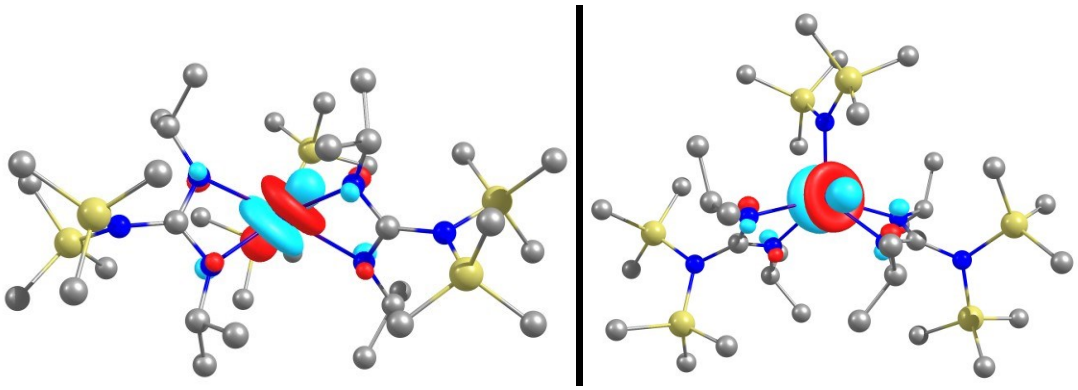

Figure S56. Calculated LUMO of ground state geometry of **[3$^+$]** (gas phase) viewed from two orientations (rendered at contour value of 0.05).

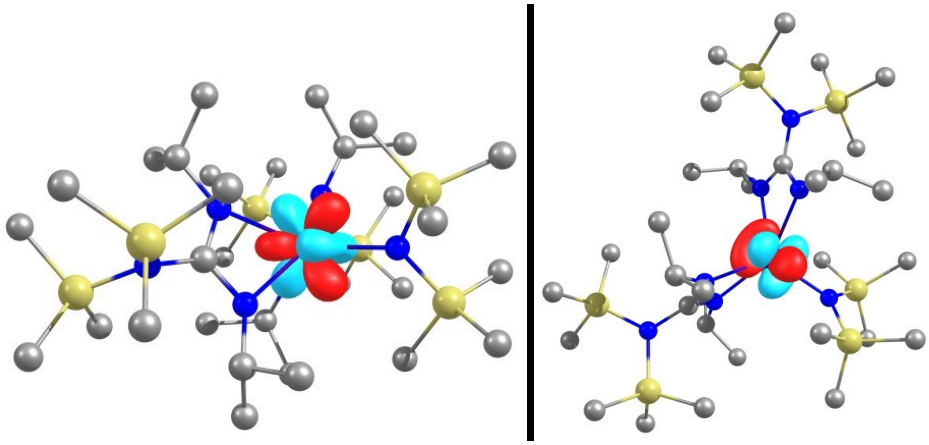

Figure S57. Calculated LUMO+1 of ground state geometry of **[3$^+$]** (gas phase) viewed from two orientations (rendered at contour value of 0.05).

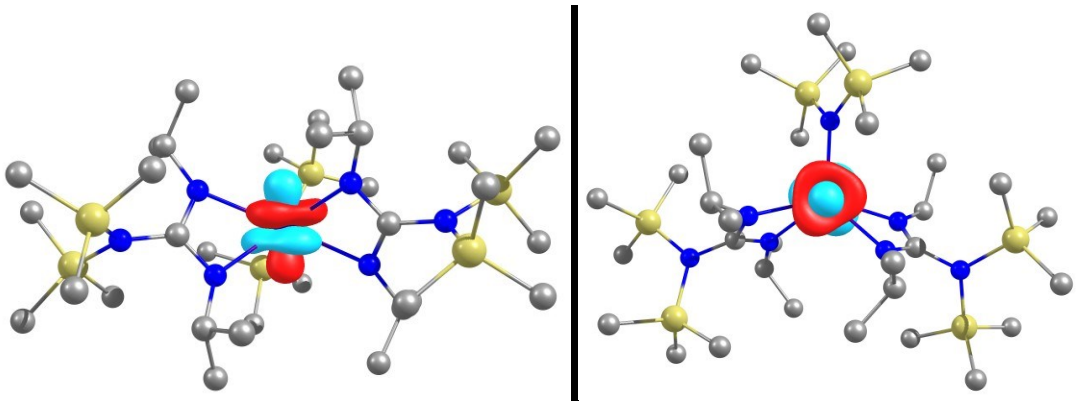

Figure S58. Calculated LUMO+2 of ground state geometry of **[3$^+$]** (gas phase) viewed from two orientations (rendered at contour value of 0.05).

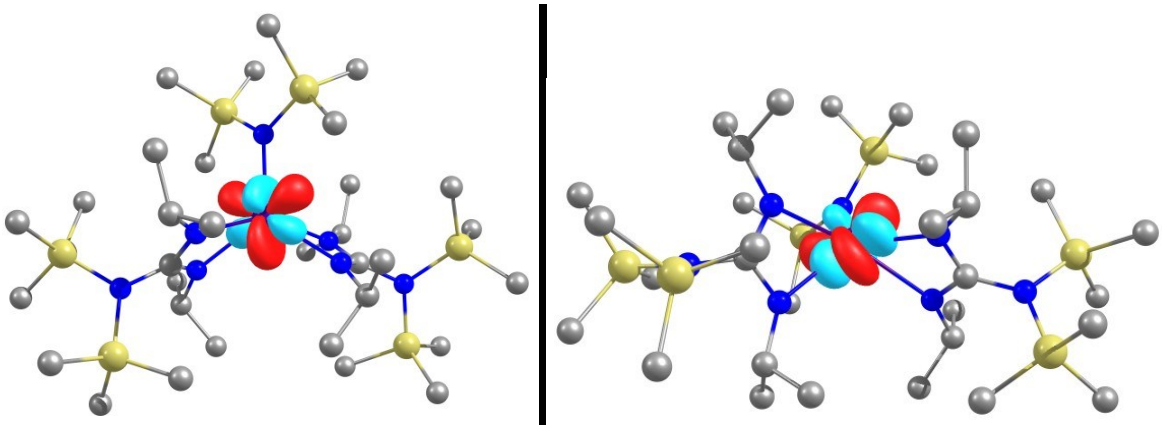

Figure S59. Calculated LUMO+3 of ground state geometry of **[3$^+$]** (gas phase) viewed from two orientations (rendered at contour value of 0.05).

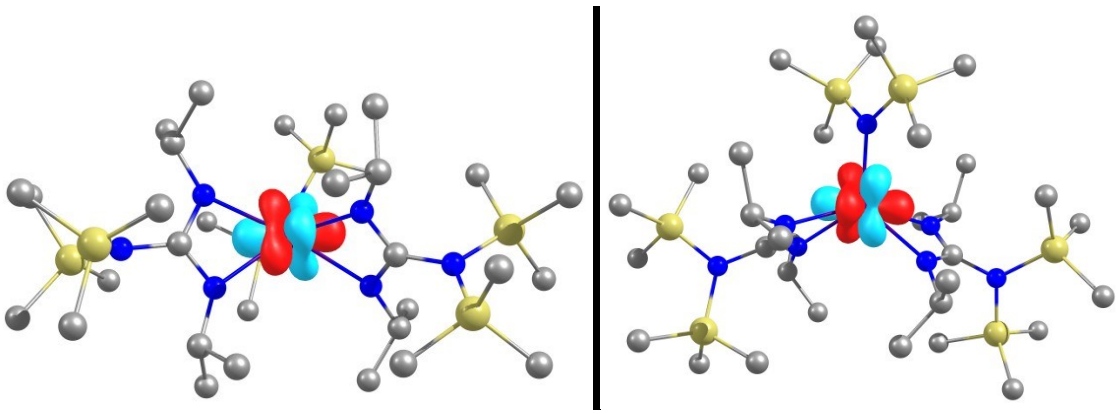

Figure S60. Calculated LUMO+4 of ground state geometry of **[3$^+$]** (gas phase) viewed from two orientations (rendered at contour value of 0.05).

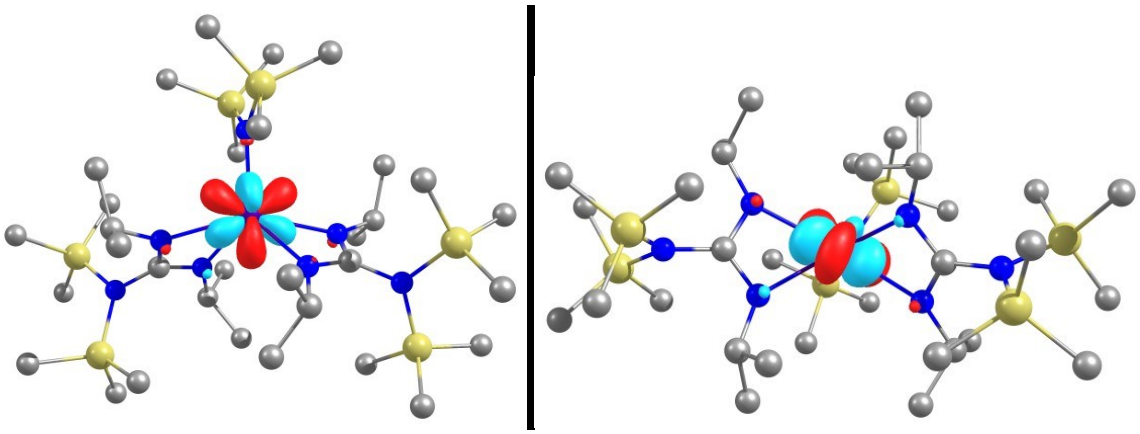

Figure S61. Calculated LUMO+5 of ground state geometry of **[3$^+$]** (gas phase) viewed from two orientations (rendered at contour value of 0.05).

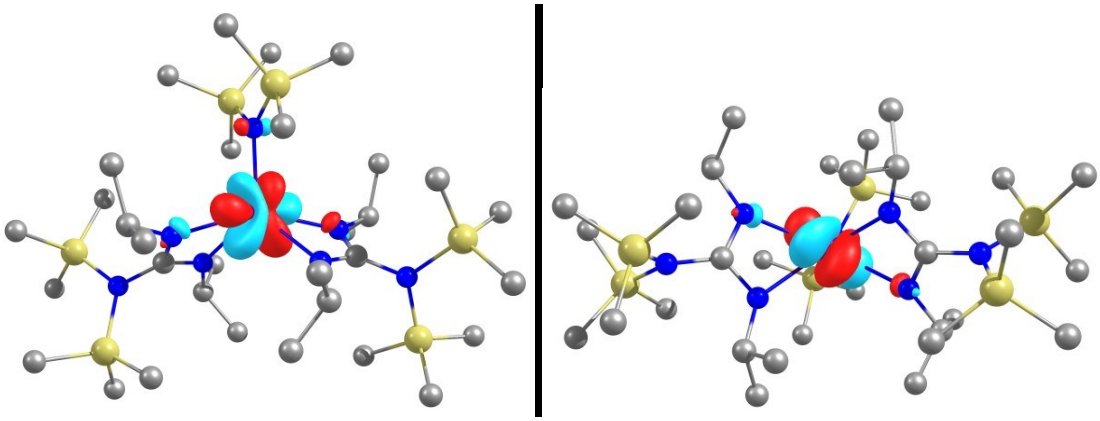

Figure S62. Calculated LUMO+6 of ground state geometry of **[3$^+$]** (gas phase) viewed from two orientations (rendered at contour value of 0.05).

Table S17. The major orbital contributions of the lowest energy vertical excitation for **[4$^+$]**

	Energy (eV)	Osc. Strength	Contributions
[4$^+$]	1.46	0.0009	HOMO-1 → LUMO+3 (17%) HOMO-1 → LUMO+4 (30%) HOMO → LUMO+5 (19%) HOMO-2 → LUMO+4 (2%) HOMO-2 → LUMO+5 (3%) HOMO-2 → LUMO+6 (2%) HOMO-1 → LUMO+1 (3%) HOMO → LUMO+1 (4%)

			HOMO → LUMO+3 (2%) HOMO → LUMO+4 (4%) HOMO → LUMO+6 (5%)
	1.47	0.001	HOMO-2 → LUMO+3 (14%) HOMO-2 → LUMO+4 (19%) HOMO → LUMO+4 (31%) HOMO → LUMO+6 (13%) HOMO-2 → LUMO (4%) HOMO-1 → LUMO+5 (3%) HOMO-1 → LUMO+6 (2%) HOMO → LUMO (4%) HOMO → LUMO+3 (3%)
	1.52	0.0171	HOMO-2 → LUMO (19%) HOMO-2 → LUMO+4 (32%) HOMO-1 → LUMO+1 (23%) HOMO → LUMO (11%) HOMO-2 → LUMO+1 (5%) HOMO-1 → LUMO (5%)
	1.53	0.0172	HOMO-2 → LUMO+1 (22%) HOMO-1 → LUMO (24%) HOMO-1 → LUMO+4 (22%) HOMO → LUMO+1 (13%) HOMO-2 → LUMO (5%) HOMO-2 → LUMO+2 (3%) HOMO-1 → LUMO+1 (4%)
	1.56	0.0011	HOMO-2 → LUMO+5 (18%) HOMO-1 → LUMO+6 (22%) HOMO → LUMO+5 (22%) HOMO-2 → LUMO+2 (4%) HOMO-2 → LUMO+3 (7%) HOMO-1 → LUMO+2 (3%) HOMO-1 → LUMO+3 (7%) HOMO → LUMO+1 (5%)

			HOMO → LUMO+6 (9%)
	1.57	0.0038	HOMO-2 → LUMO+6 (24%) HOMO-1 → LUMO+5 (22%) HOMO → LUMO+6 (13%) HOMO-2 → LUMO+2 (2%) HOMO-2 → LUMO+3 (7%) HOMO-1 → LUMO+2 (6%) HOMO-1 → LUMO+3 (5%) HOMO → LUMO (9%) HOMO → LUMO+5 (9%)
	1.61	0.0218	HOMO-2 → LUMO+2 (11%) HOMO-1 → LUMO+4 (12%) HOMO → LUMO+1 (25%) HOMO → LUMO+5 (38%) HOMO-1 → LUMO+6 (2%) HOMO → LUMO (3%) HOMO → LUMO+6 (2%)
	1.62	0.0207	HOMO-2 → LUMO+4 (13%) HOMO → LUMO (19%) HOMO → LUMO+6 (48%) HOMO-1 → LUMO+2 (9%) HOMO-1 → LUMO+6 (2%) HOMO → LUMO+1 (3%)

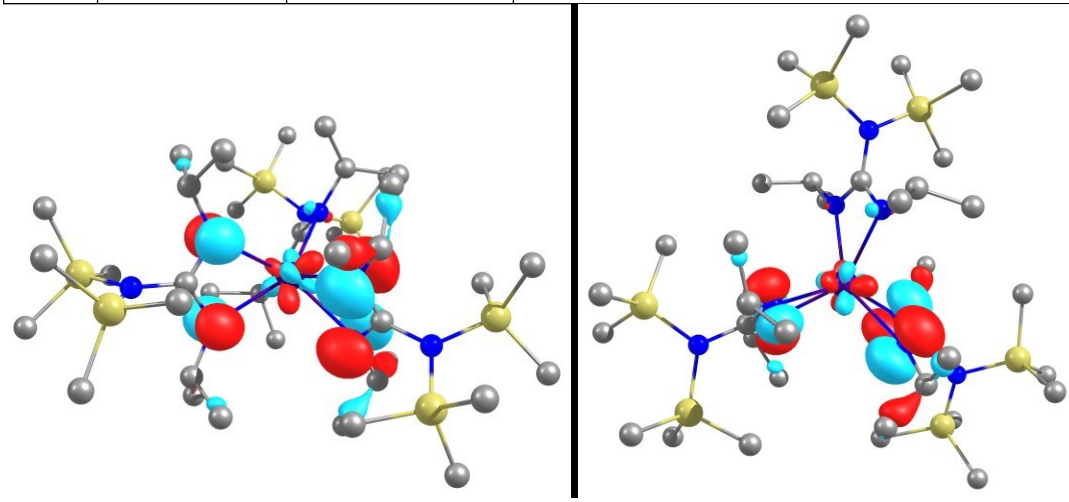

Figure S63. Calculated HOMO-2 of ground state geometry of **[4$^+$]** (gas phase) viewed from two orientations (rendered at contour value of 0.05).

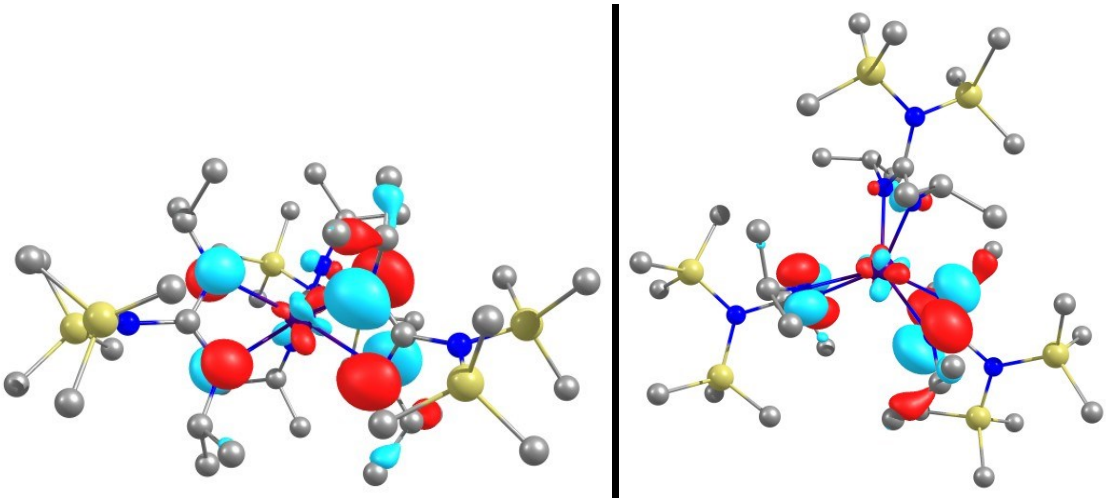

Figure S64. Calculated HOMO-1 of ground state geometry of **[4$^+$]** (gas phase) viewed from two orientations (rendered at contour value of 0.05).

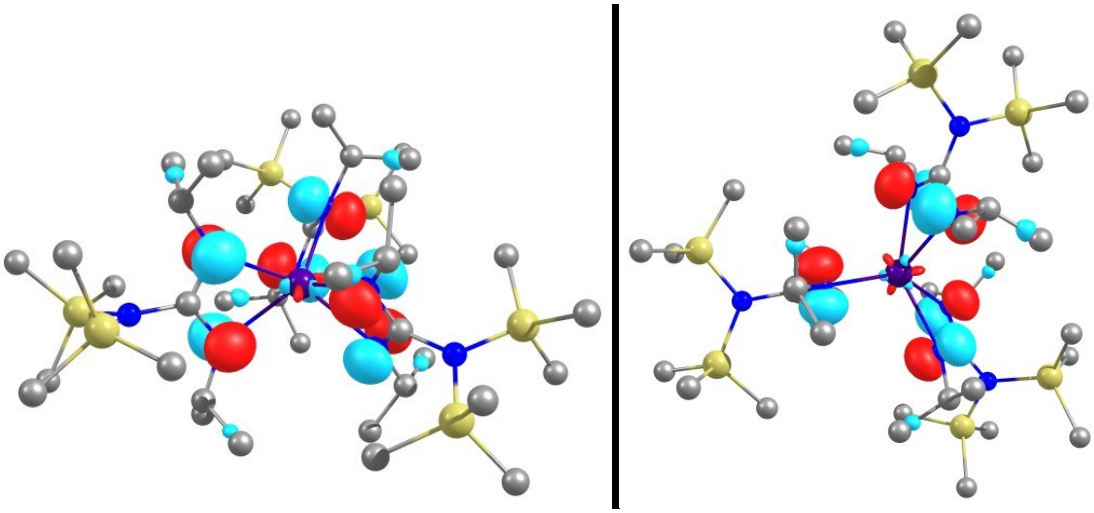

Figure S65. Calculated HOMO of ground state geometry of **[4$^+$]** (gas phase) viewed from two orientations (rendered at contour value of 0.05).

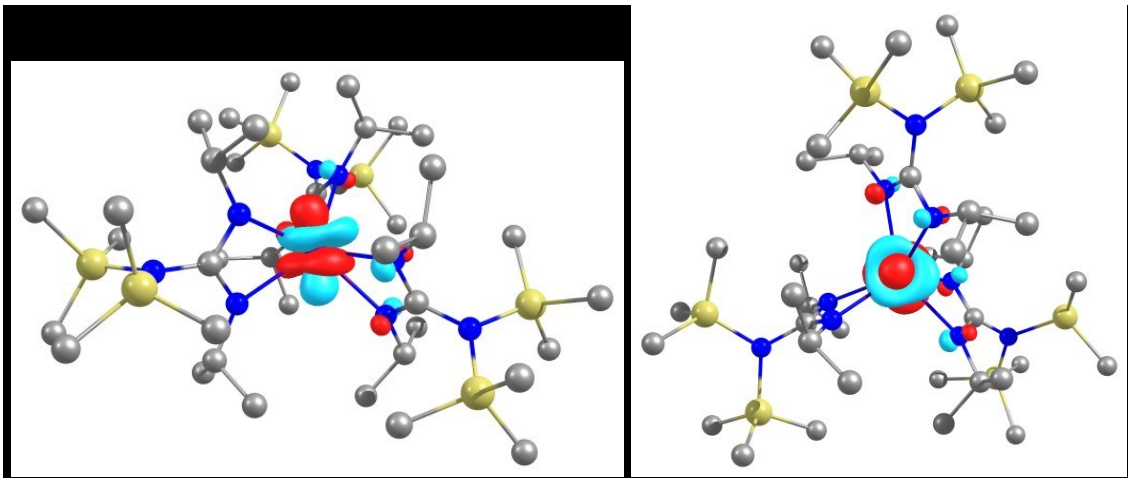

Figure S66. Calculated LUMO of ground state geometry of **[4$^+$]** (gas phase) viewed from two orientations (rendered at contour value of 0.05).

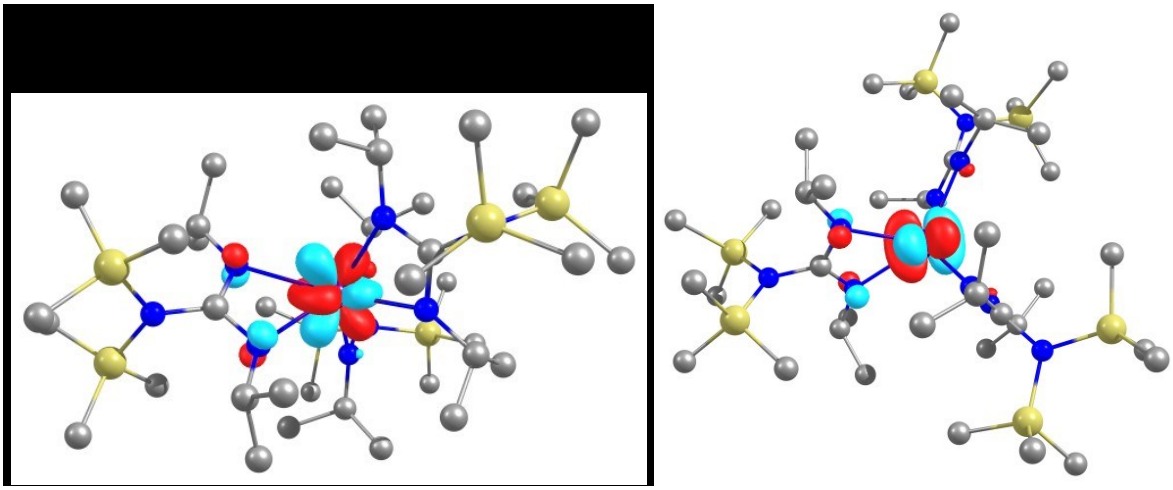

Figure S67. Calculated LUMO+1 of ground state geometry of **[4$^+$]** (gas phase) viewed from two orientations (rendered at contour value of 0.05).

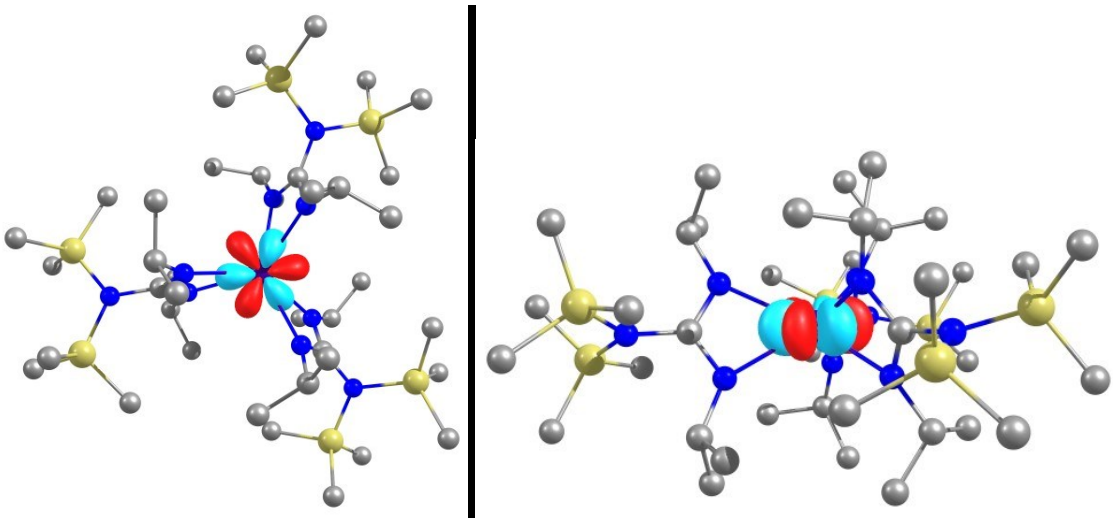

Figure S68. Calculated LUMO+2 of ground state geometry of **[4$^+$]** (gas phase) viewed from two orientations (rendered at contour value of 0.05).

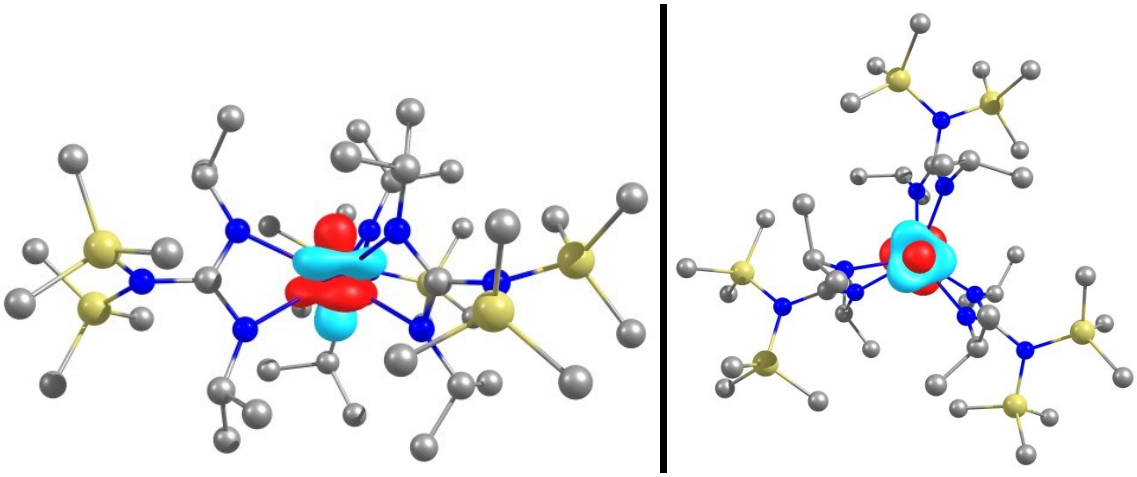

Figure S69. Calculated LUMO+3 of ground state geometry of **[4$^+$]** (gas phase) viewed from two orientations (rendered at contour value of 0.05).

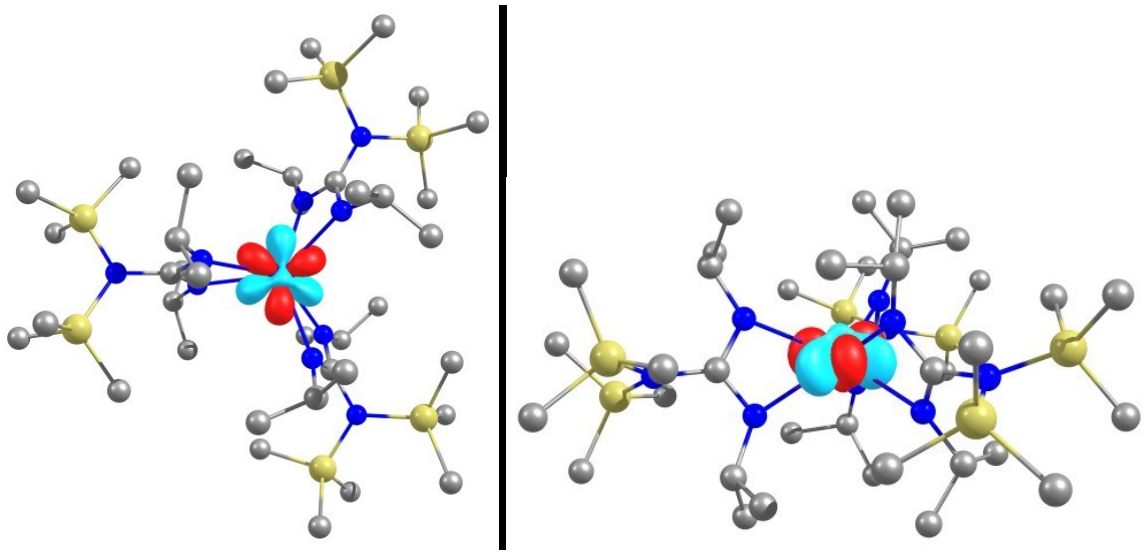

Figure S70. Calculated LUMO+4 of ground state geometry of **[4$^+$]** (gas phase) viewed from two orientations (rendered at contour value of 0.05).

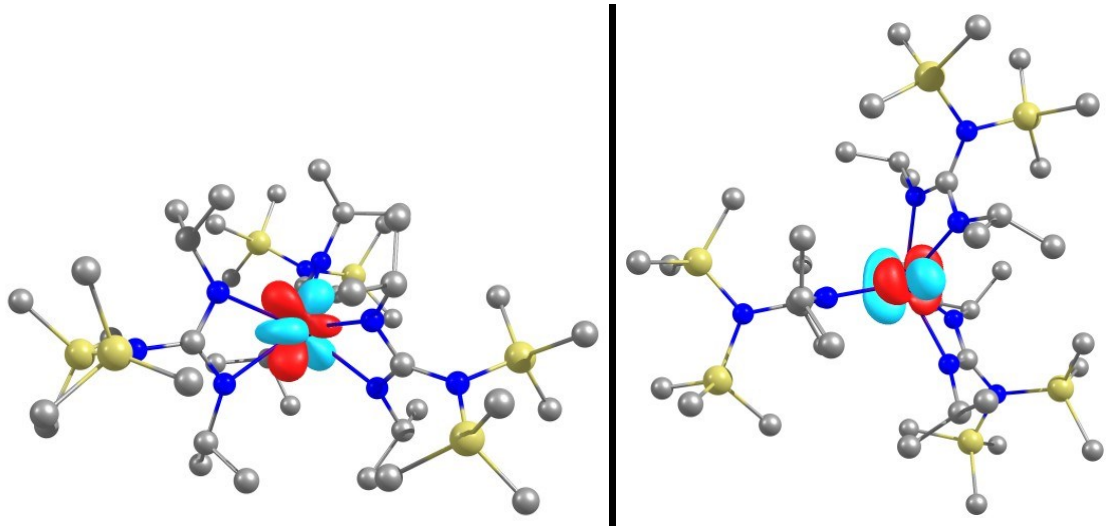

Figure S71. Calculated LUMO+5 of ground state geometry of **[4$^+$]** (gas phase) viewed from two orientations (rendered at contour value of 0.05).

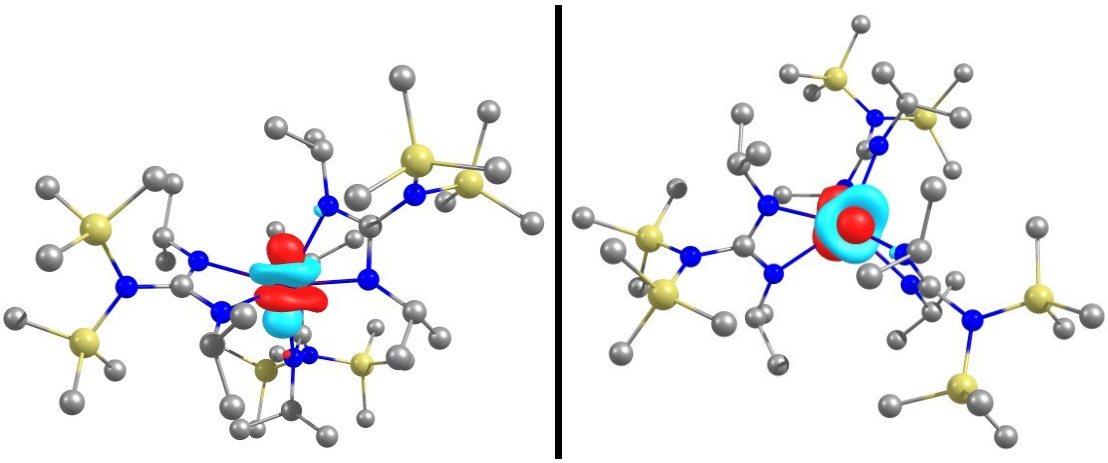

Figure S72. Calculated LUMO+6 of ground state geometry of **[4$^+$]** (gas phase) viewed from two orientations (rendered at contour value of 0.05).

Table S18. % contribution of amide, guanidinate and Ce AO character in HOMOs and LUMOs of **1-Cl, 2-Cl, [3$^+$], and [4$^+$].**

	1-Cl	**2-Cl**	**[3$^+$]**	**[4$^+$]**
amide p in HOMO	88.12	**-**	**-**	**-**
guanidinate p in HOMO	-	82.61	85.26	89.28
Ce 4f in HOMO	9.80	5.02	5.65	1.95
Ce 5d in HOMO	0.13	1.12	2.77	3.26
Ce 4f in LUMO	92.84	93.57	90.76	89.83
Ce 5d in LUMO	1.11	0.79	0.03	0.31

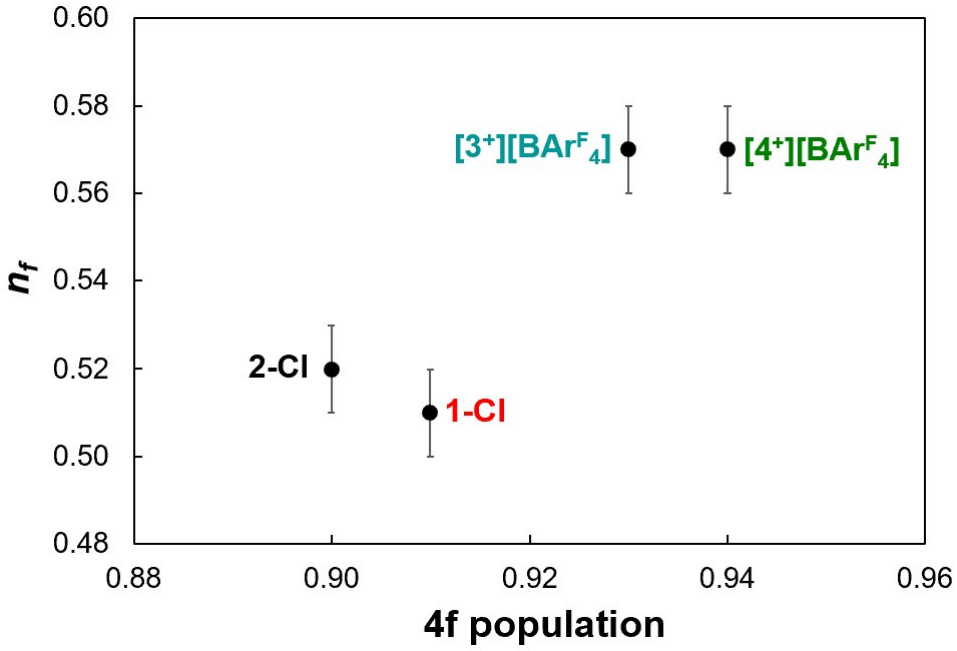

Figure S73. A plot of the n_f value and the 4f population calculated by PBE-DFT. Error bars were given for n_f values.

10. References

(1) Wojdyr, M. *J. Appl. Crystallogr.* 2010, **43**, 1126-1128.

(2) Arnold, P. L.; Turner, Z. R.; Kaltsoyannis, N.; Pelekanaki, P.; Bellabarba, R. M.; Tooze, R. P. *Chem. Eur. J.* 2010, **16**, 9623-9629.

(3) Williams, U. J.; Carroll, P. J.; Schelter, E. J. *Inorg. Chem.* 2014, **53**, 6338-6345.

(4) Yin, H.; Carroll, P. J.; Anna, J. M.; Schelter, E. J. *J. Am. Chem. Soc.* 2015, **137**, 9234-9237.

(5) Yin, H.; Carroll, P. J.; Manor, B. C.; Anna, J. M.; Schelter, E. J. *J. Am. Chem. Soc.* 2016, **138**, 5984-5993.

(6) Chávez, I.; Alvarez-Carena, A.; Molins, E.; Roig, A.; Maniukiewicz, W.; Arancibia, A.; Arancibia, V.; Brand, H.; Manuel Manríquez, J. *J. Organomet. Chem.* 2000, **601**, 126-132.

(7) Thomson, R. K.; Scott, B. L.; Morris, D. E.; Kiplinger, J. L. *C. R. Chim.* 2010, **13**, 790-802.

(8) *SAINT*; Bruker AXS Inc.: Madison, WI, 2009.

(9) *SHELXTL*; Bruker AXS Inc.: Madison, WI, 2009.

(10) Sheldrick, G. M.: *SADABS*; University of Göttingen: Göttingen, Germany, 2007.

(11) Sheldrick, G. M.: *TWINABS*; University of Göttingen: Göttingen, Germany, 2008.

(12) Sheldrick, G. *Acta Crystallogr., Sect. A* 2008, **64**, 112-122.

(13) Booth, C. H.; Walter, M. D.; Kazhdan, D.; Hu, Y.-J.; Lukens, W. W.; Bauer, E. D.; Maron, L.; Eisenstein, O.; Andersen, R. A. *J. Am. Chem. Soc.* 2009, **131**, 6480-6491.

(14) Booth, C. H.; Kazhdan, D.; Werkema, E. L.; Walter, M. D.; Lukens, W. W.; Bauer, E. D.; Hu, Y.-J.; Maron, L.; Eisenstein, O.; Head-Gordon, M.; Andersen, R. A. *J. Am. Chem. Soc.* 2010, **132**, 17537-17549.

(15) Halbach, R. L.; Nocton, G.; Booth, C. H.; Maron, L.; Andersen, R. A. *Inorg. Chem.* 2018, **57**, 7290-7298.

(16) Bain, G. A.; Berry, J. F. *J. Chem. Educ.* 2008, **85**, 532.

(17) Ward, A. L.; Buckley, H. L.; Lukens, W. W.; Arnold, J. *J. Am. Chem. Soc.* 2013, **135**, 13965-13971.

(18) Frisch, M. J.; Trucks, G. W.; Schlegel, H. B.; Scuseria, G. E.; Robb, M. A.; Cheeseman, J. R.; Scalmani, G.; Barone, V.; Mennucci, B.; Petersson, G. A.; Nakatsuji, H.; Caricato, M.; Li, X.; Hratchian, H. P.; Izmaylov, A. F.; Bloino, J.; Zheng, G.; Sonnenberg, J. L.; Hada, M.; Ehara, M.; Toyota, K.; Fukuda, R.; Hasegawa, J.; Ishida, M.; Nakajima, T.; Honda, Y.; Kitao, O.; Nakai, H.; Vreven, T.; Montgomery Jr., J. A.; Peralta, J. E.; Ogliaro, F.; Bearpark, M. J.; Heyd, J.; Brothers, E. N.; Kudin, K. N.; Staroverov, V. N.; Kobayashi, R.; Normand, J.; Raghavachari, K.; Rendell, A. P.; Burant, J. C.; Iyengar, S. S.; Tomasi, J.; Cossi, M.; Rega, N.; Millam, N. J.; Klene, M.; Knox, J. E.; Cross, J. B.; Bakken, V.; Adamo, C.; Jaramillo, J.; Gomperts, R.; Stratmann, R. E.; Yazyev, O.; Austin, A. J.; Cammi, R.; Pomelli, C.; Ochterski, J. W.; Martin, R. L.; Morokuma, K.; Zakrzewski, V. G.; Voth, G. A.; Salvador, P.; Dannenberg, J. J.; Dapprich, S.; Daniels, A. D.; Farkas, Ö.; Foresman, J. B.; Ortiz, J. V.; Cioslowski, J.; Fox, D. J.: *Gaussian 09, Revision A.02*; Gaussian, Inc.: Wallingford, CT, USA, 2009.

(19) Dolg, M.; Stoll, H.; Preuss, H. *J. Chem. Phys.* 1989, **90**, 1730-1734.

(20) Gorelsky, S. I.; Lever, A. B. P. *J. Organomet. Chem.* 2001, **635**, 187-196.

(21) Gorelsky, S. I.: *AOMix: Program for Molecular Orbital Analysis*; http://www.sg-chem.net/, University of Ottawa, version 6.5, 2011.

(22) http://chemcraftprog.com/.

(23) Marenich, A. V.; Ho, J.; Coote, M. L.; Cramer, C. J.; Truhlar, D. G. *Phys. Chem. Chem. Phys.* 2014, **16**, 15068-15106.

(24) Roos, B. O.; Taylor, P. R.; Sigbahn, P. E. M. *Chem. Phys.* 1980, **48**, 157-173.

(25) Siegbahn, P. E. M.; Almlöf, J.; Heiberg, A.; Roos, B. O. *J. Chem. Phys.* 1981, **74**, 2384-2396.

(26) Roos, B. O. *J. Quantum. Chem. Symp.* 1980, **18**, 175-189.
(27) Siegbahn, P.; Heiberg, A.; Roos, B.; Levy, B. *Phys. Scr.* 1980, **21**, 323-327.
(28) Douglas, M.; Kroll, N. M. *Annals of Physics* 1974, **82**, 89-155.
(29) Jansen, G.; Hess, B. A. *Phys. Rev. A* 1989, **39**, 6016-6017.
(30) Reiher, M.; Wolf, A. *J. Chem. Phys.* 2004, **121**, 10945-10956.
(31) Lenthe, E. v.; Baerends, E. J.; Snijders, J. G. *J. Chem. Phys.* 1993, **99**, 4597-4610.
(32) van Lenthe, E.; van Leeuwen, R.; Baerends, E. J.; Snijders, J. G. *Int. J. Quantum Chem* 1996, **57**, 281-293.
(33) Perdew, J. P.; Burke, K.; Ernzerhof, M. *Phys. Rev. Lett.* 1996, **77**, 3865-3868.
(34) Vetere, V.; Adamo, C.; Maldivi, P. *Chem. Phys. Lett.* 2000, **325**, 99-105.
(35) Stephens, P. J.; Devlin, F. J.; Chabalowski, C. F.; Frisch, M. J. *J. Phys. Chem.* 1994, **98**, 11623-11627.
(36) Duignan, T. J.; Autschbach, J. *J. Chem. Theory Comput.* 2016, **12**, 3109-3121.
(37) Fdez. Galván, I.; Vacher, M.; Alavi, A.; Angeli, C.; Aquilante, F.; Autschbach, J.; Bao, J. J.; Bokarev, S. I.; Bogdanov, N. A.; Carlson, R. K.; Chibotaru, L. F.; Creutzberg, J.; Dattani, N.; Delcey, M. G.; Dong, S. S.; Dreuw, A.; Freitag, L.; Frutos, L. M.; Gagliardi, L.; Gendron, F.; Giussani, A.; González, L.; Grell, G.; Guo, M.; Hoyer, C. E.; Johansson, M.; Keller, S.; Knecht, S.; Kovačević, G.; Källman, E.; Li Manni, G.; Lundberg, M.; Ma, Y.; Mai, S.; Malhado, J. P.; Malmqvist, P. Å.; Marquetand, P.; Mewes, S. A.; Norell, J.; Olivucci, M.; Oppel, M.; Phung, Q. M.; Pierloot, K.; Plasser, F.; Reiher, M.; Sand, A. M.; Schapiro, I.; Sharma, P.; Stein, C. J.; Sørensen, L. K.; Truhlar, D. G.; Ugandi, M.; Ungur, L.; Valentini, A.; Vancoillie, S.; Veryazov, V.; Weser, O.; Wesołowski, T. A.; Widmark, P.-O.; Wouters, S.; Zech, A.; Zobel, J. P.; Lindh, R. *J. Chem. Theory Comput.* 2019, **15**, 5925-5964.
(38) ADF2014, SCM, Theoretical Chemistry, Vrije Universiteit, Amsterdam, The Netherlands. http://www.scm.com.
(39) Roos, B. O.; Lindh, R.; Malmqvist, P.-Å.; Veryazov, V.; Widmark, P.-O.; Borin, A. C. *J. Phys. Chem. A* 2008, **112**, 11431-11435.
(40) Roos, B. O.; Lindh, R.; Malmqvist, P.-Å.; Veryazov, V.; Widmark, P.-O. *J. Phys. Chem. A* 2004, **108**, 2851-2858.
(41) Widmark, P.-O.; Malmqvist, P.-Å.; Roos, B. O. *Theor. Chim. Acta* 1990, **77**, 291-306.
(42) Van Lenthe, E.; Baerends, E. J. *J. Comput. Chem.* 2003, **24**, 1142-1156.
(43) Glendening, E. D.; Badenhoop, J. K.; Reed, A. E.; Carpenter, J. E.; Bohmann, J. A.; Morales, C. M.; Landis, C. R.; Weinhold, F.: *NBO 6.0*; Theoretical Chemistry Institute, University of Wisconsin: Madison, 2013.